Contrib Mineral Petrol (2011) 162:573–597
DOI 10.1007/s00410-011-0613-8

ORIGINAL PAPER

The importance of fractional crystallization and magma mixing in controlling chemical differentiation at Süphan stratovolcano, eastern Anatolia, Turkey

Yavuz Özdemir · Jon Blundy · Nilgün Güleç

Received: 2 July 2010 / Accepted: 23 January 2011 / Published online: 11 February 2011

Abstract Süphan is a 4,050 m high Pleistocene-age stratovolcano in eastern Anatolia, Turkey, with eruptive products consisting of transitional calc-alkaline to mildly alkaline basalts through trachyandesites and trachytes to rhyolites. We investigate the relative contributions of fractional crystallization and magma mixing to compositional diversity at Süphan using a combination of petrology, geothermometry, and melt inclusion analysis. Although major element chemistry shows near-continuous variation from basalt to rhyolite, mineral chemistry and textures indicate that magma mixing played an important role. Intermediate magmas show a wide range of pyroxene, olivine, and plagioclase compositions that are intermediate between those of basalts and rhyolites. Mineral thermometry of the same rocks yields a range of temperatures bracketed by rhyolite (~750°C) and basalt (~1,100°C). The linear chemical trends shown for most major and trace elements are attributed to mixing processes, rather than to liquid lines of descent from a basaltic parent. In contrast, glassy melt inclusions, hosted by a wide range of phenocryst types, display curved trends for most major elements, suggestive of fractional crystallization. Comparison of these trends to experimental data from basalts and trachyandesites of similar composition to those at Süphan indicates that melt inclusions approximate true liquid lines of descent from a common hydrous parent at pressures of ~500 MPa. Thus, the erupted magmas are cogenetic, but were generated at depths below the shallow, pre-eruptive magma storage region. We infer that chemical differentiation of a mantle-derived basalt occurred in the mid- to lower crust beneath Süphan. A variety of more and less evolved melts with ≥55 wt% SiO_2 then ascended to shallow level where they interacted. The presence of glomerocrysts in many lavas suggests that cogenetic plutonic rocks were implicated in the interaction process. Blending of diverse, but cogenetic, minerals, and melts served to obscure the true liquid lines of descent in bulk rocks. The fact that chemical variation in melt inclusions preserves deep-seated chemical differentiation indicates that inclusions were trapped in phenocrysts prior to shallow-level blending. Groundmass glasses evolved after mixing and display trends that are distinct from those of melt inclusions.

Keywords Süphan · Eastern Anatolia · Petrology · Melt inclusion · Magma mixing · Fractional crystallization

Communicated by T. L. Grove.

Electronic supplementary material The online version of this article (doi:10.1007/s00410-011-0613-8) contains supplementary material, which is available to authorized users.

Y. Özdemir · J. Blundy
Department of Earth Sciences, University of Bristol,
Wills Memorial Building, Bristol BS8 1 RJ, UK

Y. Özdemir (✉) · N. Güleç
Department of Geological Engineering,
Middle East Technical University,
06531 Ankara, Turkey
e-mail: yozdemir@metu.edu.tr

Introduction

Reconstructing the magmatic plumbing systems of volcanoes is one of the principal goals of igneous petrology, with attendant implications for understanding and mitigating volcanic hazard. Of particular interest is the interplay between regions of magma generation and magma storage, which may be displaced in both place and time. A number of authors (e.g., Hildreth and Moorbath 1988; Grove et al. 2005; Annen et al. 2006) have proposed that generation of silicic and intermediate magmas commonly occurs in the

deep crust through crystallization of mantle-derived basalts and assimilation of older crustal material. This is in marked contrast to magma storage regions beneath many volcanoes that are typically at depths of several km, and may be controlled by volatile saturation pressures. In such a situation, cogenetic magmas generated at the same depth in the crust may ascend and interact with each other at shallow levels. Subvolcanic magma storage regions then become loci of extensive blending between petrogenetically related magmas of contrasted compositions and their crystalline residua (e.g., Dungan and Davidson 2004; Reubi and Blundy 2009).

In this paper, we report petrological results from Süphan, a stratovolcano in eastern Turkey that shows an exceptionally wide range of erupted magma types from a series of closely spaced vents. We use a combination of mineral chemistry, geothermometry, and melt inclusion analysis to unravel the relative importance of magma crystallization and mixing processes in generating compositional diversity.

Background and regional geology

The eastern Anatolian region (eastern Turkey) is one of the best examples of a continental collision zone in the world. It also comprises one of the high plateaus of the Alpine–Himalayan Mountain Belt with an average elevation of ~2 km above sea level. The plateau attained its current elevation in about the Middle Miocene when the collision between the Eurasian and Arabian plates terminated along the Bitlis Suture Zone (Dewey et al.1986; Şengör and Kidd 1979). Almost two thirds of the plateau (~40,000 km^2) is covered by the products of collision-related volcanism (Aydar et al. 2003; Keskin et al. 1998; Keskin 2007; Notsu et al. 1995; Pearce et al. 1990; Şen et al. 2004; Şengör et al. 2008; Yılmaz et al. 1987, 1998). With the exception of a few volcano-stratigraphy studies (Karaoğlu et al. 2005; Özdemir et al. 2006, 2007; Yılmaz et al. 1998), previous works on the eastern Anatolian volcanics are geochemically oriented (Ercan et al. 1990; Innocenti et al. 1976, 1980; Kheirkhah et al. 2009; Keskin et al. 1998; Keskin 2003, 2007; Notsu et al. 1995; Pearce et al. 1990; Şengör et al. 2008; Yılmaz et al. 1987, 1998), and mostly concerned with an overall evaluation of collision-related volcanism on a regional scale, rather than a systematic study of individual volcanic centers and their petrology.

Collision-related volcanic rocks in eastern Anatolia extend from Erzurum-Kars Plateau in the northern part of the region to the Arabian foreland in the south (Fig. 1).

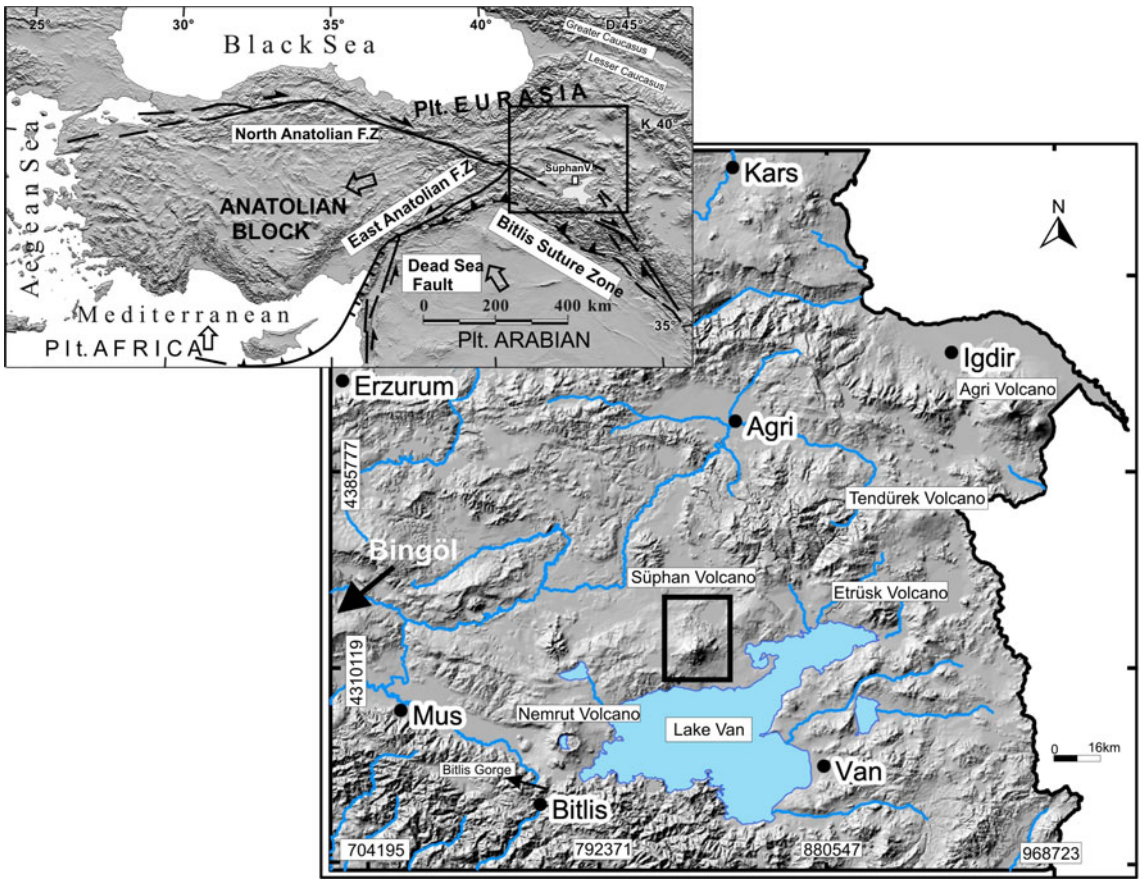

Fig. 1 Tectonic setting and location map of Süphan stratovolcano

Ages of volcanic rocks in the region range from 11 Ma (Keskin 2003) to AD 1441 (Tchalenko 1977). A series of large shield and stratovolcanoes is present in eastern Anatolia, including Ağrı, Süphan, Nemrut, Tendürek, Etrüsk, and many secondary eruption centers. Collision-related volcanic rocks of eastern Anatolia span the entire compositional range from basalt to rhyolite (Keskin 2007; Notsu et al. 1995; Özdemir et al. 2006; Pearce et al. 1990; Şengör et al. 2008). Major and trace element compositional diversity is large, ranging from calc-alkaline types resembling active continental margins to alkali basalts with intraplate characteristics (Pearce et al. 1990). The volcanic units of Erzurum-Kars Plateau and Ağrı are calc-alkaline, whereas those of the Muş-Nemrut-Tendürek volcanics are alkaline to mildly alkaline in character (Keskin et al. 1998; Özdemir et al. 2006; Pearce et al. 1990). Lavas from Bingöl and Süphan display transitional chemical characteristics (Pearce et al. 1990). Keskin (2003) proposed a decrease in age and an increase in the alkaline nature of the volcanics from north to south across the region.

Results from geophysical studies in eastern Anatolia indicate that the crust has an average thickness of ~45 km and the mantle lithosphere is thin (Angus et al. 2006; Özacar et al. 2008) or absent (Gok et al. 2007; Sandvol et al. 2003a, b; Şengör et al. 2003; Zor et al. 2003) across a considerable portion of the region. Based on geophysical findings, Şengör et al. (2003) suggested that the steepening and breakoff of a northward subducting slab belonging to the northern branch of the Neo-Tethyan ocean allowed hot, partially molten asthenosphere to be emplaced near the base of the crust. Şengör et al. (2008) proposed the source of the volcanics in eastern Anatolia to be a combination of both undepleted asthenosphere and subduction-modified mantle wedge. Recently, Kheirkhah et al. (2009) suggested instead that most of the volcanics are derived from a lithospheric source after the partial loss of the lower lithosphere, breakoff of the Tethyan lithospheric slab, or a combination of the two.

Süphan stratovolcano (lat. 38°55′N, long. 42°59′E), located to the north of Lake Van, is one of the largest Quaternary volcanoes in eastern Anatolia, rising to a summit elevation of 4,050 m. The volcanic center is located at the intersection of two major fault zones, trending NE–SW and NW–SE (Yılmaz et al. 1998). Volcanic products of Süphan are exposed over an area of ~2,000 km^2. Reported ages range between 2.0 and 0.1 Ma (Innocenti et al. 1976; Notsu et al. 1990; Pearce et al. 1990; Yılmaz et al. 1998). Initial products of Süphan volcanism were silicic plinian eruptions deposited over Middle Miocene limestone and alternating with lacustrine sediments, possibly Pliocene–Pleistocene in age, which suggests that a shallow lake basin occupied the entire region at the onset of volcanic activity (Yılmaz 1998). The oldest lava flows observed around the volcano are rhyolitic obsidians with reported K–Ar ages of 0.76 ± 0.56 Ma (Ogata et al. 1989). These silicic units (plinian eruptions and rhyolitic obsidian flows) are overlain by an effusive phase, which includes basaltic, basaltic trachyandesitic, trachyandesitic, and trachytic lava flows, and extends several kilometers around the volcano. Pearce et al. (1990) reported K–Ar ages of the trachytic lavas in this phase as ranging between 0.36 ± 0.15 and 0.23 ± 0.19 Ma. This eruptive phase is responsible for the construction of the main stratocone. The basic and intermediate products are overlain by deposits of several plinian eruptions and a block and ash flow which extends ~10 km away from the southeastern parts of the volcano. After this explosive phase, an extrusive phase developed on the summit and the flanks of the main cone includes dacitic and rhyolitic domes. The most recent product of volcanism is phreatomagmatic and includes a rhyolitic maar at the volcano's southern edge.

Analytical methods

Whole-rock major element compositions were determined by ICP emission spectrometry following a lithium metaborate/tetraborate fusion and dilute nitric acid digestion at ACME analytical laboratories. Trace element contents were determined in the same laboratory by ICP mass spectrometry following a lithium metaborate/tetrabortate fusion and nitric acid digestion. Minerals and glasses were analyzed by electron microprobe (EMPA) at the University of Bristol using a CAMECA SX-100 five-spectrometer (WDS) instrument. Minerals were analyzed using a 20 kV accelerating voltage, 10 nA beam current, and a 5 μm beam diameter. Groundmass glasses and melt inclusions were analyzed using a 15 kV accelerating voltage, 2–4 nA beam current, and a 15 μm beam diameter to minimize alkali migration (Humphreys et al. 2006). Calibration was carried out on a variety of natural and synthetic minerals and glasses. Data reduction used the PAP routine.

Whole-rock compositions

A total of 60 samples were analyzed for their whole-rock compositions. Representative analyses are shown in Table 1; the full dataset can be found in Supplementary Table 1. Volcanic products of Süphan cover a broad compositional spectrum from basalt to rhyolite, with SiO_2 ranging from 51.5 to 74.8 wt% (anhydrous). MgO contents range between 7.15 and 0.02 wt%, with mg# between 0.56 and 0.05. On the basis of total alkali vs. silica (TAS, Le Bas et al. 1986; Fig. 2a), Süphan volcanic rocks straddle the transition between subalkaline and alkaline character. The

Table 1 Representative major and trace element contents of Süphan volcanics

Sample	2006 99	2006 112	2006 76	2006 1	2006 130	2005 68	2006 86	2005 59	2006 6	2006 77
Rock type	Basalt	Basaltic trachyandesite					Trachyandesite			
SiO_2 (%)	51.47	52.09	54.70	54.97	54.33	54.31	58.86	58.52	60.31	60.44
TiO_2	1.92	2.02	1.89	1.96	2.28	2.35	1.68	1.17	1.29	0.99
Al_2O_3	17.44	16.95	16.64	17.01	15.93	15.77	15.81	16.12	16.53	16.09
Fe_2O_3	10.98	9.97	10.37	9.98	11.12	11.27	8.30	8.92	7.18	8.36
MgO	7.15	4.42	3.53	3.39	2.94	3.05	2.36	1.91	2.40	1.37
CaO	9.19	7.47	6.46	6.07	6.30	6.22	4.99	4.70	5.11	4.47
Na_2O	4.01	4.35	4.09	4.00	3.76	3.99	4.54	4.38	4.45	4.26
K_2O	0.90	1.67	1.87	2.00	2.12	2.07	2.44	2.68	2.19	3.06
P_2O_5	0.36	0.44	0.39	0.36	0.44	0.41	0.28	0.61	0.26	0.46
MnO	0.17	0.14	0.17	0.17	0.18	0.18	0.13	0.16	0.12	0.14
LOI	0.00	0.20	−0.10	0.10	0.60	0.30	0.40	0.30	0.10	0.40
Total	103.63	99.75	100.01	100.01	100.00	99.92	99.81	99.47	99.94	100.04
Sr (ppm)	355.7	342.3	296.9	269.2	272.2	257.0	219.8	230.5	230.1	245.5
Rb	19.4	41	58.1	58.6	63.7	61.2	80.3	80.3	64.9	100.9
Ba	150	272	333.8	312.1	419.1	368.5	308.0	419.7	319.6	547.9
Ni	59.5	34.8	5.4	5.1	4.7	4.8	4.7	0.9	3.6	0.8
Sc	29	21	21	22	22	23	17	15	16	15
Co	42.3	32.1	36.1	31.4	31.6	32	25.1	22.5	23.9	20.3
Cs	0.1	0.5	2	1.9	2	2	2.8	2.7	1.6	3.4
Ga	18.2	19.3	20.8	20.4	22.7	21.9	19.7	22.3	17.8	23.7
Th	2.6	6.0	9.3	9.4	10	10.4	8.4	10.5	8.1	13.4
Ta	0.6	0.9	1.2	1.1	1.2	1.2	0.8	1.5	0.9	1.5
Nb	9.3	15.7	15.5	14.8	17.5	17.7	9.5	17.5	9.2	20.1
U	0.8	1.7	2.4	2.5	2.6	2.5	3.4	3.3	2.7	3.9
Zr	191.7	268.8	293.1	274.2	315.3	302.9	303.8	341.4	236.1	395.4
Hf	4.8	6.4	7.5	6.9	8.1	7.5	7.6	9	6.2	10.1
Y	32.8	38.3	45.3	42.3	48.9	45.9	45.8	54.1	34.1	58.9
Ce	36.1	58.2	68.5	64.4	74.6	69.4	49.3	77.7	47.4	96.3
Nd	22.9	33.2	35.4	32.0	37.7	37.5	30.5	42.6	24.4	49.3
Sm	5.18	6.73	7.9	7.4	8.9	8.1	6.88	9.4	5.4	10.5
Eu	1.62	1.91	2.05	1.88	2.22	2.19	1.85	2.44	1.44	2.4
Gd	5.73	6.95	8.02	7.49	8.41	8.31	7.5	9.47	5.8	9.7
Tb	0.98	1.19	1.51	1.35	1.66	1.49	1.27	1.73	1.06	1.87
Dy	5.53	6.69	8.08	7.3	8.6	8.09	7.45	9.57	5.97	9.88
Ho	1.23	1.4	1.5	1.54	1.61	1.65	1.63	1.89	1.25	1.8
Er	3.42	3.94	4.78	4.6	5.12	4.78	4.64	5.34	3.68	5.81
Tm	0.51	0.59	0.7	0.66	0.75	0.68	0.71	0.8	0.52	0.87
Pr	5.11	7.75	8.93	8.11	9.61	8.79	6.73	9.97	5.88	12.1
Yb	3.15	3.48	4.08	3.89	4.65	4.2	4.45	4.76	3.32	4.93
La	16.2	27.4	29.5	29.1	33.3	31.5	22	34.5	21	42.8
Lu	0.47	0.53	0.65	0.62	0.69	0.66	0.67	0.76	0.53	0.76

Table 1 continued

Sample	2006 81	2006 105	2006 8	2005 10	2008 4	2006 59	2005 28	2006 110	2005 52	2005 69	2007 5
Rock type	Trachyandesite			Trachyte			Dacite		Rhyolite		
SiO_2 (%)	58.94	60.63	61.49	62.77	64.11	65.49	65.11	64.97	72.79	74.81	72.91
TiO_2	1.52	0.97	0.86	0.92	0.87	0.68	0.82	0.77	0.15	0.08	0.18
Al_2O_3	16.17	15.95	15.80	15.56	15.70	15.73	15.28	15.40	13.71	13.52	13.92
Fe_2O_3	8.35	7.96	8.15	6.16	5.73	5.02	5.16	5.18	1.40	1.41	1.58
MgO	2.36	1.53	1.17	1.47	1.38	0.96	1.29	1.25	0.30	0.04	0.27
CaO	5.31	4.25	3.80	4.32	3.60	2.95	3.50	3.43	1.29	0.54	1.21
Na_2O	4.20	4.30	4.34	4.83	4.72	3.67	4.29	4.46	3.75	4.25	4.05
K_2O	2.23	3.04	3.13	2.48	2.61	2.13	2.96	2.89	4.44	4.91	4.23
P_2O_5	0.28	0.47	0.40	0.30	0.27	0.23	0.24	0.28	0.06	0.03	0.05
MnO	0.13	0.15	0.16	0.11	0.11	0.10	0.09	0.10	0.06	0.03	0.06
LOI	0.40	0.80	0.60	1.00	0.70	0.80	1.20	1.10	1.80	0.20	1.30
Total	99.89	100.05	99.90	99.92	99.80	97.76	99.94	99.84	99.75	99.82	99.80
Sr (ppm)	242.3	221.1	188.2	193.3	188.9	169.9	188.0	198.2	83.8	16.5	87.0
Rb	61.9	91	93.9	69.9	80.8	96.9	93.8	84.2	105.0	132.9	106.7
Ba	336.7	489.8	445.5	320.9	344.7	429.8	446.4	440	1,017.5	440.8	925.0
Ni	1.7	0.9	0.5	0.5	0.6	0.6	1.3	1.2	1.6	0.2	1
Sc	15	15	17	11	10	8	10	9	4	3	4
Co	26.4	18.5	13.6	16.9	17.3	15.4	15.8	11.4	6.5	15	27.1
Cs	2.4	3.1	3.2	2.5	2.9	3.8	2.9	2.5	2.5	4.9	2.5
Ga	19.3	23.1	21.6	20.3	19.9	19.5	19.5	17.9	15.3	15.9	15
Th	7.6	12.1	11.8	10.1	11.0	12.6	11.9	12.2	20.3	15.9	21.8
Ta	0.9	1.5	1.4	0.9	0.9	1.1	1.4	1.4	2.3	1.2	2.4
Nb	10.3	18.2	18.3	10.1	9.4	11.9	16.5	17.9	26.3	8	26.5
U	2.7	3.5	3.5	3.4	3.6	4.4	4.2	4.5	7.3	4.6	7.4
Zr	256.1	385.4	385.4	298.2	320.2	355.6	292.1	309.2	109.8	106.5	147.3
Hf	7	9.7	9.8	7.4	8.6	9	8.1	7.6	4.1	4	5.1
Y	39.3	56.1	56	39.5	40.2	44.6	41.1	40.5	37	26	40.5
Ce	49.3	86.0	83.2	53.6	53.8	62.1	66.9	61.8	72.7	58.4	96.6
Nd	25.7	45	44.5	28	27.5	31.3	33.2	32.8	29.3	23.2	39.4
Sm	6.2	9.9	9.5	6.3	6.3	6.6	6.6	6.67	5.8	4.6	7.14
Eu	1.71	2.57	2.39	1.73	1.55	1.65	1.52	1.7	1.2	0.45	1.39
Gd	6.33	9.86	9.88	6.67	6.45	7.09	6.85	6.78	5.81	4.32	6.84
Tb	1.26	1.89	1.77	1.29	1.22	1.29	1	1.17	1.13	0.83	1.18
Dy	6.56	9.74	9.65	7.15	7.07	7.5	7	6.53	6.34	4.5	6.69
Ho	1.21	1.85	2	1.37	1.42	1.53	1.38	1.46	1.19	0.89	1.42
Er	4.01	6.12	5.91	4.1	4.18	4.88	4.1	4.16	3.72	2.64	4.24
Tm	0.62	0.93	0.9	0.62	0.61	0.72	0.61	0.63	0.58	0.38	0.65
Pr	6.37	11.06	10.73	6.81	6.81	7.86	8.23	7.71	8.17	6.54	10.95
Yb	3.69	5.2	5.26	3.86	3.97	4.27	3.91	3.99	3.67	2.62	4.11
La	21.5	37.4	36.9	24.1	24.1	28	32.6	29.9	37.3	28	49.4
Lu	0.57	0.81	0.84	0.59	0.62	0.72	0.61	0.61	0.55	0.41	0.60

majority of volcanics plot on the subalkaline field of Miyashiro (1978) and Irvine and Baragar (1971). However, some of them plot on the alkaline-subalkaline division line of Miyashiro (1978) and a few of them within the alkaline field. The lavas with mildly alkaline character are older and overall the character of the volcanism turns to transitional and subalkaline with time. Subalkaline lavas of the volcano are classified as high-K calc-alkaline (Gill 1981). Figure 2 shows selected major and trace element (Sr) variation diagrams for whole rocks. Compositions span a wide range

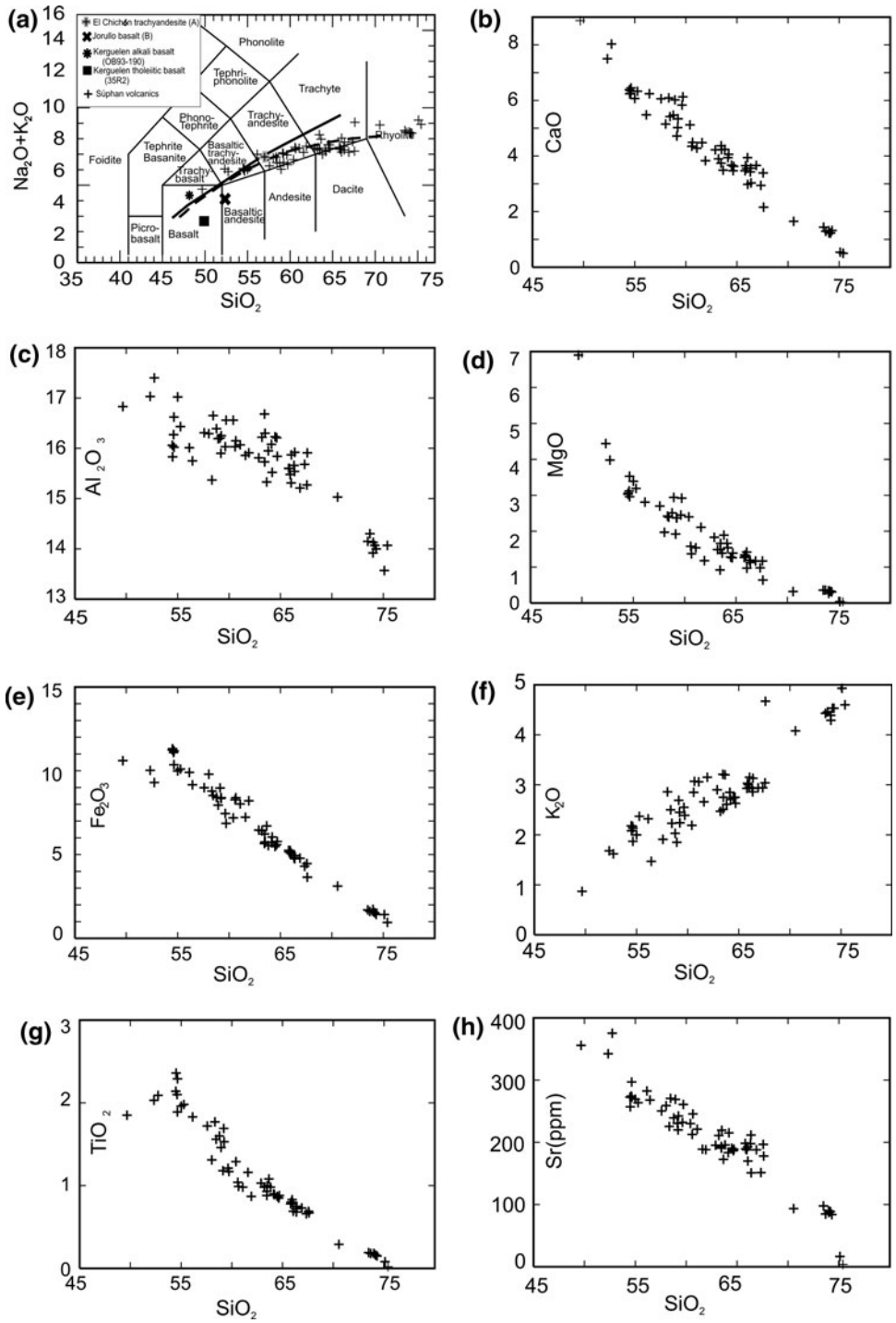

Fig. 2 Major and selected trace element variation diagrams of Süphan whole rocks. **a** TAS diagram (Le Bas et al. 1986) of the Süphan volcanics and starting compositions of different experimental studies discussed in text. Subalkaline-alkaline divisions of TAS diagram are from Miyashiro (1978) (*dashed line*) and Irvine and Baragar (1971) (*solid line*). **b** CaO; **c** Al_2O_3; **d** MgO; **e** Fe_2O_3; **f** K_2O; **g** TiO_2; **h** Sr

in SiO_2, with little evidence of a compositional gap, except possibly in the range 67–73 wt% SiO_2, where there is only one analysis. Al_2O_3, CaO, Fe_2O_3, MgO, TiO_2, and Sr display good negative correlations with SiO_2,whereas K_2O and total alkalies have positive correlations with SiO_2. The well-defined correlations of major and trace elements would appear to reflect the continuous operation of chemical differentiation processes at Süphan. It is striking that most trends are linear with SiO_2, in the range 55–70 wt% SiO_2. At lower and higher SiO_2, there is some evidence of curvature in Al_2O_3, Fe_2O_3, TiO_2, and MgO. Establishing the extent to which the observed trends are the products of fractional crystallization, as opposed to mixing processes or crustal assimilation is a key objective of this paper.

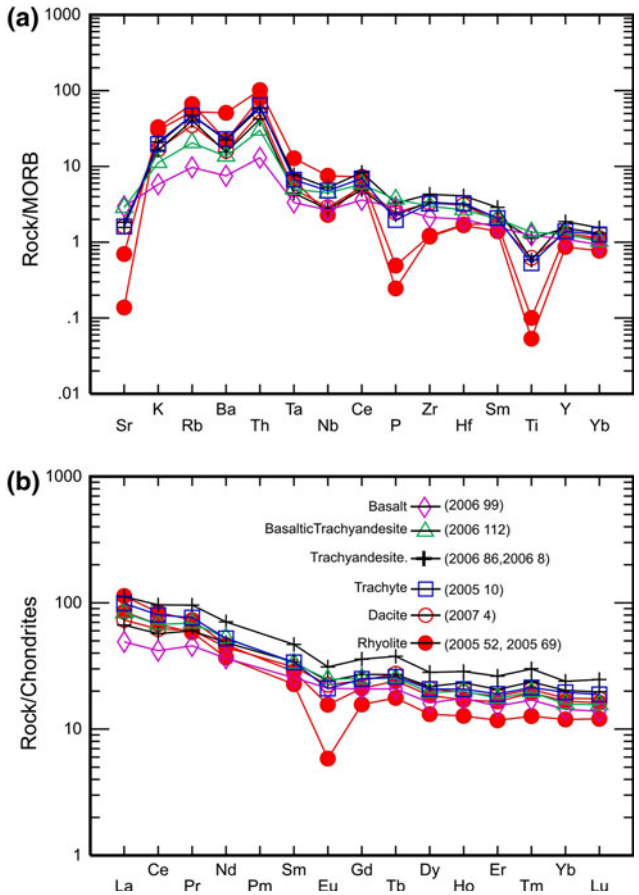

Fig. 3 **a** MORB-normalized (Pearce 1983) multielement patterns of selected Süphan volcanics. **b** Chondrite-normalized (Nakamura 1974) REE patterns of selected Süphan volcanics

MORB-normalized trace element and chondrite-normalized REE patterns of selected Süphan volcanics are shown in Fig. 3a and b, respectively. All samples show similar MORB-normalized trace element patterns (Fig. 3a) characterized by enrichment (relative to MORB) of both large-ion lithophile (LILE) and high field strength (HFSE) elements, although the former are more pronounced than the latter. Sr, Ba, P, and Ti in the intermediate-felsic members have distinctive negative anomalies compared to mafic members. The depletion of Nb and Ta points to the presence of an inherited subduction component in the mantle source. The chondrite-normalized REE patterns (Fig. 3b) reveal enrichment of light rare earth elements (LREE) over heavy rare earth elements (HREE). $(La/Yb)_N$ ratio is 3.4 for basaltic rocks and increases slightly with increasing SiO_2: 4.8–5.3 for basaltic trachyandesites, 3.3–5.8 for trachyandesites, 3.6–4.7 for trachytes, 4.6–5.6 for dacites, and 5.7–8.0 for rhyolites. The MREE to HREE remain remarkably flat over this interval. Patterns for all rocks are approximately parallel, but the highest REE concentrations occur in intermediate rocks (trachyandesites) rather than at the high or low SiO_2 end-members. The magnitude of negative Eu anomaly increases with increasing SiO_2.

Petrography

Samples from Süphan included in this study range in composition from basalt to rhyolite. All samples are typically crystal-rich and porphyritic with hyalopitic groundmass, although only the basaltic sample is entirely crystalline. The groundmass glass is dark brown to black in mafic rocks and light brown to colorless in felsic rocks.

A single basalt, from a lava flow exposed at the southern part of the volcano (Sample No: 2006-99), was studied. This rock contains euhedral and subhedral mm-sized *plagioclase + clinopyroxene + olivine* phenocrysts in a groundmass consisting of plagioclase, clinopyroxene, olivine, and Fe–Ti oxide microcrysts. Pyroxene and plagioclase display typically glomeroporphyritic and subophitic textures. Olivines are the most common mafic mineral and are iddingsitized along their rims.

Basaltic trachyandesitic lavas consist of *plagioclase + olivine +clinopyroxene ± orthopyroxene* phenocrysts. The groundmass contains plagioclase, pyroxene, olivine, opaque microlites, and glass. Plagioclase phenocrysts rocks are unzoned or slightly oscillatory zoned, and display patchy and sieve textures. The unzoned or slightly oscillatory zoned plagioclases (Fig. 4a) range up to 1 cm in size. Plagioclases with sieve-textured rims have small melt inclusions (Fig. 4b). Patchy-textured crystals have an irregular corroded core with abundant large melt and mineral inclusions (pyroxene and Fe–Ti oxides). The amount of olivine is less than that in basalts. Some olivines are replaced by clinopyroxene and partially or totally iddingsitized (Fig. 4c). Orthopyroxenes are rare and replaced or rimmed by clinopyroxenes (Fig. 4d). Olivines, orthopyroxenes, and clinopyroxenes all have melt inclusions. Accessory apatite is found as inclusions in plagioclases.

Trachyandesitic lavas consist of *plagioclase ± olivine + clinopyroxene +orthopyroxene* phenocrysts, with groundmass plagioclase, pyroxene, opaque microlites, and glass. These lavas include crystal clots that are made of orthopyroxene, clinopyroxene plagioclase, and opaque minerals (Fig. 4e). Most plagioclases, clinopyroxenes, orthopyroxenes, and olivines contain melt inclusions. Orthopyroxenes are the most common mafic mineral. Olivines, with iddingsitized rims, occur rarely.

Trachytic lavas consist of *plagioclase + clinopyroxene +orthopyroxene ± amphibole +Fe–Ti oxide* phenocrysts set in a groundmass consisting of plagioclase, clinopyroxene, amphibole, Fe–Ti oxides, and glass. These lavas are characterized by vesicular, intersertal, and trachytic

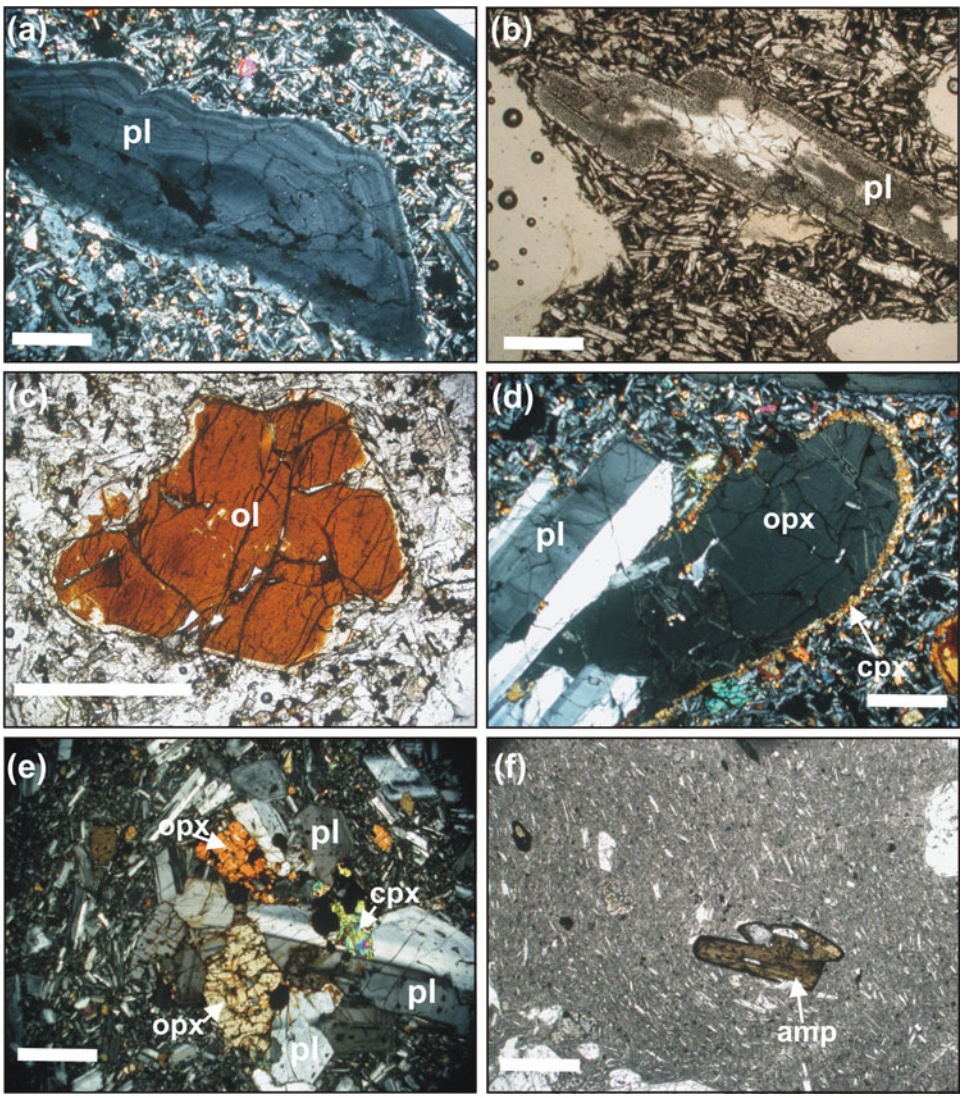

Fig. 4 Petrographic features of Süphan volcanics **a** Euhedral oscillatory zoned plagioclase (*pl*) in basaltic trachyandesite (Sample No.; 2006-112). **b** Sieve-textured plagioclase in basaltic trachyandesite (Sample No.; 2005-68). **c** Iddingsitized olivine (*ol*) phenocryst in basaltic trachyandesite (Sample No.; 2006-112). **d** Orthopyroxene (*opx*) phenocryst rimmed by clinopyroxene (*cpx*) in basaltic trachyandesite (Sample No.; 2006-112). **e** Crystal clot from trachyandesitic lava flow, containing orthopyroxene, clinopyroxene, plagioclase, and Fe–Ti oxides (Sample No.; 2006-6). **f** Amphibole (*amp*) phenocryst replaced by Fe–Ti oxides along their rims in trachytic lava flow (Sample No.; 2008-4). *Scale bars* represent 1 mm

textures. Most of the phenocryst phases have melt inclusions. Orthopyroxenes are more abundant than clinopyroxenes, some of which are opacitized along their rims. Crystals clots of plagioclase, clinopyroxene, orthopyroxene, and Fe–Ti oxides are common. Some of the plagioclases have corroded rims. Trachytes mark the first occurrence of amphiboles, which are characteristically reddish and completely replaced or rimmed by Fe–Ti oxides (Fig. 4f). Apatite is found as an accessory phase.

Dacitic rocks occur as domes only. They consist of *plagioclase + clinopyroxene + orthopyroxene + amphibole ± biotite + Fe–Ti oxides* and colorless glass. The amount of clinopyroxene is reduced compared to mafic and intermediate lavas; amphibole is the most abundant mafic mineral. Most phenocrysts have melt inclusions. Plagioclases have sieve texture; zircon and apatite occur as accessories.

Rhyolitic lavas, having vitrophyric and seriate textures, are mainly composed of *plagioclase ± orthopyroxene + amphibole + biotite + quartz + K-feldspar + Fe–Ti oxides*. Orthopyroxenes are rare and found only in the older rhyolitic obsidian flows. Biotite is the most common mafic mineral phase; K-feldspars and quartz are relatively rare.

Mineral chemistry

In order to illustrate the evolution of mineral chemistry with changing host rock SiO_2 contents, we present analyses as a series of stacked histograms ranked downwards in order of increasing SiO_2 (Fig. 5). Selected mineral data are presented in Tables 2, 3, 4, 5 and 6; the full dataset can be found in Supplementary Table 2.

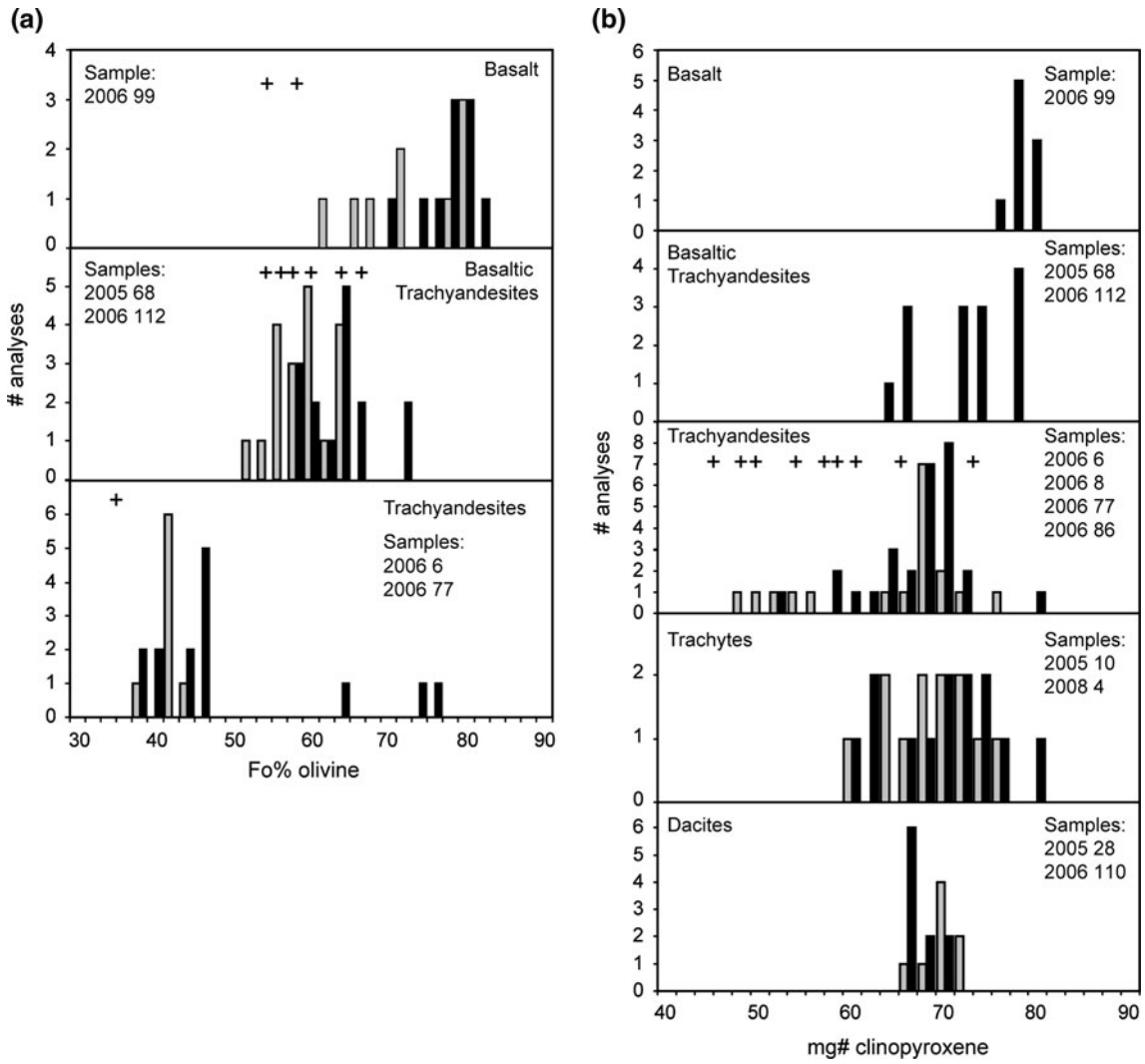

Fig. 5 Frequency distribution diagrams for core, rim, and microlite compositions of olivine (**a**), clinopyroxene (**b**), orthopyroxene (**c**), and plagioclase (**d**) grouped according to host rock composition. *Black colored bars* indicate core compositions, *gray colored bars* indicate rim compositions, *crosses* indicate microlites

Olivine

Olivine (Table 2; Fig. 5a) occurs in basalt, basaltic trachyandesites, and trachyandesites as euhedral to subhedral phenocrysts. All crystals are normally zoned with forsterite (Fo)-rich cores. Olivine compositions (core, rim, and microlite) display a wide range: $Fo_{53–80}$ for basalts; $Fo_{52–71}$ for basaltic trachyandesites; and $Fo_{37–75}$ for trachyandesites. Olivine microlite compositions have the lowest Fo in basalts, whereas microlites in basaltic trachyandesites overlap with phenocryst compositions. Fo decreases, in general, from basalt to trachyandesite. However, one trachyandesitic sample (2006-6,) contains olivine with core compositions (Fo_{75}) similar to those in basalt.

Clinopyroxene

Clinopyroxene (Table 3; Fig. 5b) is present in basalts to dacites with decreasing abundance. Clinopyroxene occurs in basaltic rocks as needle-like microcrysts, but forms phenocrysts in intermediate and silicic rocks. Most phenocrysts are augite, although diopside sometimes occurs as phenocryst rims in dacites. Augites are Ca-rich and have compositions in the range $En_{24–45}$, $Fe_{15–33}$, and $Wo_{35–44}$. Most clinopyroxenes are weakly normally zoned. The mg# [molar Mg/(Mg + Fe)] of clinopyroxenes in basalts and dacites have limited ranges of 76–80 and 64–71, respectively. However, mg# of clinopyroxenes in basaltic trachyandesites, trachyanadesites, and trachytes range widely between these two extremes.

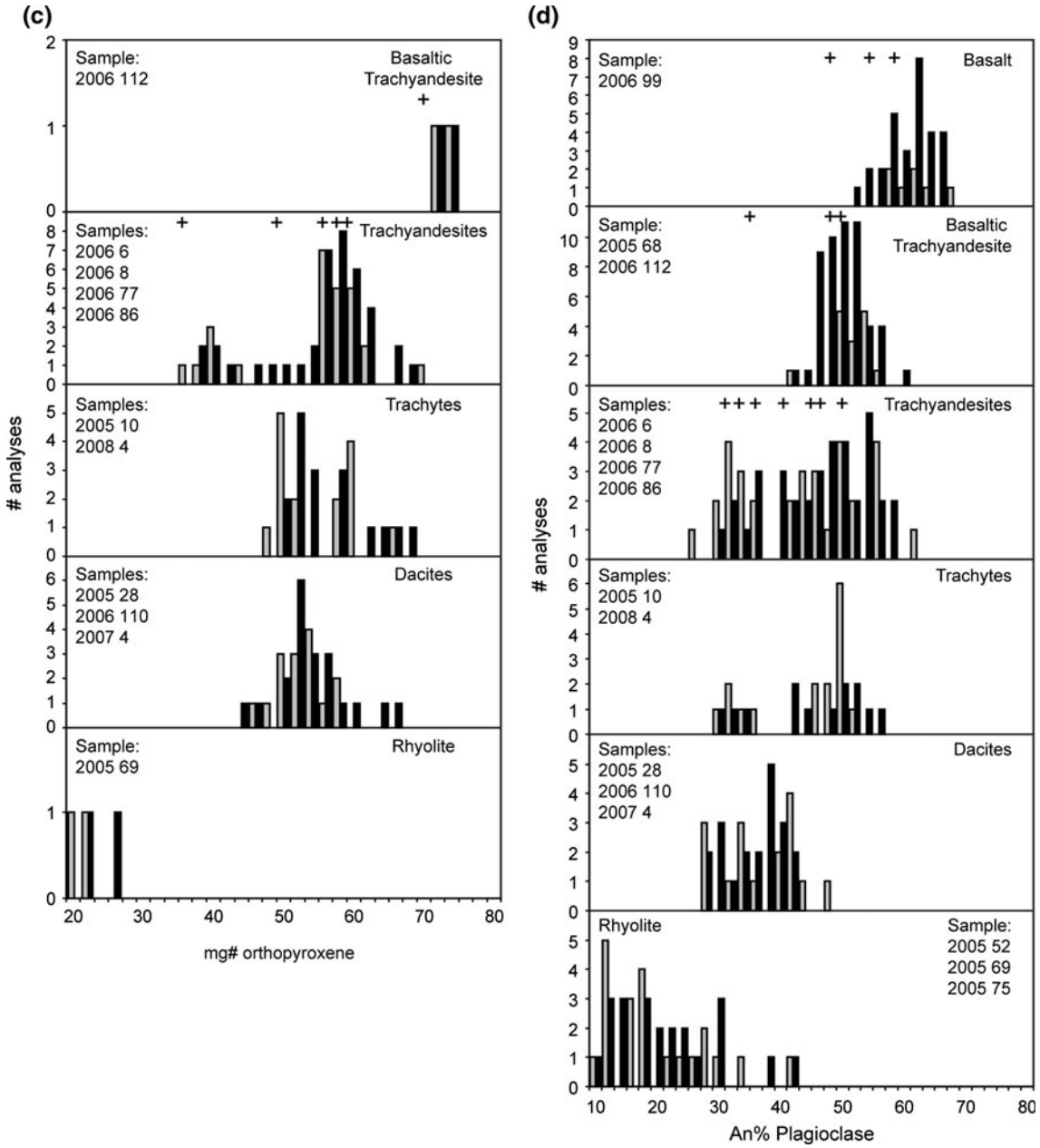

Fig. 5 continued

Orthopyroxene

Orthopyroxene (Table 3; Fig. 5c) is present in basaltic trachyandesites to rhyolites with increasing abundance. Orthopyroxenes range from enstatite to ferrosilite, with 1–4 mol% wollastonite component. Although there is quite considerable compositional overlap between samples, an older rhyolitic lava (2005-69) with distinctly lower mg# has higher FeO and lower CaO content than those from the other lavas (Supplementary Table 2, Table 3). As for clinopyroxenes, the basalts and rhyolites show relatively limited ranges in mg# (74–76 and 19–27, respectively), whereas intermediate rocks show a range between these extremes. Trachyandesite sample 2006-8 is particularly remarkable in this regard with a range in mg# from 34 to 60. Normally zoned orthopyroxene phenocrysts with Mg-rich cores often coexist with reversely zoned orthopyroxene phenocrysts with Mg-rich rims in a single rock (Samples; 2005–10, 2006–6, 2006–86, 2006–110, 2008–4).

Table 2 Representative olivine compositions

Sample	200699	200699	200699	2006112	2006112	2006112	200568	200568	200568	200677	200677	200677	20066	20066
Grain	ol2c	ol2r	ol13c	ol1c	ol1r	olm2	ol3c	ol3r	olmic5	ol5c	ol5r	olmic1	ol1c	ol2c
Crystal type	FC	FC	M	FC	FC	FC	FC	FC	M	FC	FC	M	FC	FC
Position	Core	Rim	Core	Core	Rim	Core	Core	Rim	Core	Core	Rim	Core	Core	Core
SiO_2	38.95	37.29	35.49	37.93	36.41	36.65	35.51	35.17	35.66	34.01	33.84	33.28	38.87	38.54
TiO_2	0.01	0.03	0.06	0.02	0.03	0.04	0.05	0.16	0.04	0.04	0.01	0.08	0.01	0.01
Al_2O_3	0.07	0.00	0.01	0.02	0.01	0.03	0.03	0.01	0.01	0.00	0.00	0.03	0.02	0.02
$Cr2O_3$	0.02	0.02	0.00	0.01	0.02	0.00	0.00	0.00	0.00	0.00	0.00	0.00	0.00	0.00
FeO	21.26	28.22	38.58	25.46	34.14	32.70	36.38	39.33	37.76	44.36	45.88	48.41	22.77	23.89
MnO	0.32	0.50	0.68	0.33	0.57	0.53	0.63	0.69	0.67	0.78	0.95	1.15	0.37	0.35
MgO	39.60	33.50	25.01	35.70	28.54	30.38	28.38	25.59	26.78	20.89	19.84	16.58	38.02	38.28
NiO	0.12	0.07	0.06	0.12	0.07	0.06	0.04	0.00	0.04	0.04	0.00	0.03	0.11	0.04
CaO	0.25	0.29	0.34	0.28	0.27	0.26	0.26	0.32	0.29	0.25	0.27	0.55	0.19	0.187
Total	100.60	99.92	100.24	99.88	100.04	100.65	101.28	101.28	101.24	100.37	100.81	100.10	100.36	101.33
Fo (%)	76.6	67.5	53.2	71.2	59.4	62.0	57.8	53.3	55.4	45.2	43.0	37.4	74.6	73.8

FC phenocryst-sized free crystal, *M* microlite

Table 3 Representative pyroxene compositions

Sample	200699	2006112	200568	20068	20068	200510	200510	2006110	2006112	20068	20068	20084	20074	200569	200569
Grain	cpx9c	cpx6c	cpx6	cp5c	cp5r	cp5cT	cp5rT	cpx2c	opx2c	op1r	op7c	op7c	op4c	opx1c	opx1r
Crystal type	M	FC	M	FC	FC	FC	FC	FC	FC	FC	FC	FC	FC	FC	FC
Position	Core	Core	Core	Core	Rim	Core	Rim	Core	Core	Rim	Core	Core	Core	Core	Rim
SiO_2	50.31	50.52	49.98	49.86	50.24	51.72	51.94	51.93	53.55	49.37	51.09	51.40	50.86	46.79	46.59
TiO_2	1.69	1.90	1.41	0.31	0.48	0.43	0.40	0.24	0.49	0.16	0.21	0.14	0.11	0.13	0.10
Al_2O_3	2.47	3.55	4.52	1.31	1.48	1.56	1.43	1.01	1.63	0.32	0.79	0.43	0.27	0.53	0.52
FeO	9.65	10.02	14.35	18.04	17.83	12.50	12.60	12.81	16.57	36.43	26.98	29.55	32.53	44.20	43.48
MnO	0.27	0.25	0.45	0.65	0.68	0.49	0.45	0.74	0.40	1.32	0.85	0.97	2.04	1.52	1.39
MgO	13.89	13.22	13.42	10.87	10.64	13.12	13.20	13.10	24.81	10.64	19.53	16.62	14.05	6.04	6.31
CaO	20.59	20.21	16.83	17.99	18.46	20.62	20.16	20.12	2.24	1.72	1.50	1.44	1.02	0.71	0.57
K_2O	0.01	0.04	0.07	0.09	0.01	0.01	0.02	0.01	0.01	0.00	0.02	0.03	0.00	0.01	0.00
Na_2O	0.52	0.55	1.17	0.37	0.36	0.33	0.34	0.25	0.07	0.07	0.12	0.02	0.02	0.01	0.00
Total	99.41	100.26	102.19	99.50	100.17	100.78	100.55	100.20	99.76	100.04	101.08	100.60	100.89	99.93	98.97
En	40.5	39.44	39.7	31.7	31.0	37.2	37.7	37.2	69.0	32.2	53.9	47.8	41.1	18.7	19.8
Fs	16.3	17.2	24.6	30.6	30.3	20.7	20.9	21.6	26.5	64.1	43.1	49.2	56.8	79.7	78.9
Wo	43.2	43.36	35.8	37.7	38.7	42.1	41.4	41.1	4.5	3.7	3.0	3.0	2.1	1.6	1.3
Mg #	76.0	70.79	71.7	56.7	55.0	69.3	68.1	67.5	72.7	34.3	60.1	50.6	43.6	20.1	21.0

FC phenocryst-sized free crystal, *M* microlite

Feldspars

Plagioclase (Table 4; Fig. 5d) is the most abundant phenocryst and groundmass phase in all Süphan lavas. Plagioclase phenocrysts ($An_{52–67}$) in basalt typically display reverse zoning with cores slightly more An-rich than rims. Some display weak oscillatory zoning. Microlite compositions are $An_{48–59}$ in basalts. Some plagioclase phenocrysts contain inclusions of olivine, clinopyroxene, and Fe–Ti oxides. Plagioclase in basaltic trachyandesites range between $An_{40–54}$ (phenocrysts) and $An_{36–50}$ (microlites). They also show normal, reverse, and weak oscillatory zoning. Plagioclases in trachytes and trachyandesites have similar textures to those in basaltic trachyandesites and most have melt, pyroxene, and Fe–Ti inclusions indicating relatively late crystallization of plagioclase. An content of phenocrysts displays a wide range ($An_{25–61}$ in trachyandesites; $An_{29–56}$ in trachytes); this is more apparent in samples 2006-6 and 2006-8. The majority of phenocrysts display reverse and weak oscillatory zoning. Microlite compositions

Table 4 Representative feldspar compositions

Sample	2006 99	2006 99	2006 112	2006 112	2006 86	2005 10	2005 10	2005 28	2005 28	2005 75	2005 75	2005 52	2005 52	2005 75	2005 75
Grain	pl1c	pl1r	pl12c	pl12r	pl1mic	pl5c	pl5r	pl5c	pl5r	pl3c	pl3r	kf3c	kf3r	kf6c	kf6r
Crystal type	FC	FC	FC	FC	M	FC	FC	FC	FC	FC	FC	FC	FC	FC	FC
Position	Core	Rim	Core	Rim	Core	Core	Rim	Core	Rim	Core	Rim	Core	Rim	Core	Rim
SiO_2	53.22	51.38	55.54	54.69	61.21	58.45	56.74	58.12	56.25	64.70	64.96	65.02	63.32	65.28	64.88
TiO_2	0.096	0.087	0.12	0.10	0.18	0.02	0.04	0.03	0.02	0.01	0.01	0.01	0.02	0.00	0.00
Al_2O_3	28.79	30.29	27.30	27.77	23.19	27.88	26.45	25.78	27.02	21.84	21.42	18.82	18.90	18.80	18.67
FeO	0.51	0.51	0.53	0.51	0.77	0.38	0.37	0.29	0.30	0.06	0.05	0.07	0.08	0.03	0.04
MnO	0.01	0.00	0.02	0.00	0.00	0.00	0.04	0.00	0.01	0.00	0.00	0.00	0.00	0.01	0.00
MgO	0.12	0.09	0.10	0.10	0.04	0.04	0.05	0.01	0.00	0.00	0.00	0.00	0.00	0.00	0.00
CaO	12.36	13.41	10.07	10.85	5.68	10.14	9.78	8.54	10.07	2.77	2.37	0.16	0.17	0.10	0.12
Na_2O	4.76	4.16	5.91	5.23	7.10	5.88	6.12	6.57	5.89	9.74	9.54	3.10	2.99	3.54	3.54
K_2O	0.25	0.20	0.55	0.42	1.33	0.39	0.31	0.55	0.42	0.96	1.05	11.36	10.92	11.21	11.02
Total	100.13	100.12	100.14	99.66	99.51	103.18	99.91	99.89	99.98	100.07	99.39	98.54	96.41	98.98	98.28
An	58.1	63.4	47.0	52.1	28.2	47.7	46.1	40.5	47.4	12.9	11.3	0.8	0.9	0.5	0.6
Ab	40.5	35.5	49.9	45.5	63.9	50.1	52.2	56.4	50.2	81.8	82.7	29.1	29.1	32.2	32.6
Or	1.4	1.1	3.1	2.4	7.9	2.2	1.7	3.1	2.4	5.3	6.0	70.1	70.0	67.3	66.8

FC phenocryst-sized free crystal, *M* microlite

Table 5 Representative amphibole and biotite compositions

Sample	2008 4	2008 4	2005 28	2005 28	2006 110	2006 110	2005 52	2005 52	2005 69	2005 69	2005 52	2005 52
Grain	a1c	a1r	a2c	a2r	a5c	a5r	amp1c	amp3r	bio1c	bio1r	bio2c	bio2r
Crystal type	FC	FC	FC	FC	FC	FC	FC	FC	FC	FC	FC	FC
Position	Core	Rim	Core	Rim	Core	Rim	Core	Rim	Core	Rim	Core	Rim
SiO_2	42.99	43.01	46.26	44.92	49.15	50.77	45.96	43.51	33.41	33.31	35.48	34.57
TiO_2	2.47	2.65	1.94	2.18	0.92	0.63	1.28	1.75	4.80	5.19	3.20	3.61
Al_2O_3	9.92	8.63	6.95	7.97	4.34	2.72	6.51	8.33	14.03	13.71	13.76	14.01
FeO	18.49	18.88	17.76	18.21	12.98	11.15	20.15	20.09	30.02	30.99	23.42	25.43
MnO	0.32	0.08	0.38	0.39	0.48	0.49	0.98	0.75	0.19	0.25	0.58	0.60
MgO	10.61	10.57	12.02	11.51	13.11	13.67	9.65	9.20	4.26	4.36	9.30	7.80
CaO	10.98	10.65	11.24	11.19	17.62	19.61	10.81	11.03	0.02	0.03	0.01	0.02
Na_2O	3.06	2.67	1.75	1.97	0.68	0.46	1.48	1.65	0.56	0.42	0.52	0.50
K_2O	0.64	0.69	0.642	0.861	0	0.007	0.614	0.936	8.59	8.09	8.21	8.27
Total	99.47	97.84	98.93	99.19	99.28	99.50	97.43	97.24	95.89	96.35	94.48	94.81
mg#	57.7	58.2	64.5	62.7	78.5	86	54.8	52.7	20.2	20.1	41.5	35.4

FC phenocryst-sized free crystal, *M* microlite

are $An_{27–51}$. Compositions of plagioclases in crystal clots overlap with those of phenocysts in the same sample.

The amount of the plagioclase is markedly less in dacites and rhyolites. Plagioclase compositions in dacites are in the range $An_{26–47}$, displaying oscillatory and reverse zoning. Rhyolite plagioclases are in the range $An_{9–41}$. The older rhyolitic samples (2005-69, 2005-75) have the lowest An content ($An_{10–23}$). Plagioclases in dacites and rhyolites are also found as inclusions in amphiboles and biotites.

In summary, plagioclase compositions tell a similar tale to olivine and pyroxenes, with relatively limited compositional range in the highest and lowest SiO_2 rocks and quite a wide range in intermediate rocks.

K-feldspars are only found in rhyolitic samples and are sanidine in composition (ranging between $An_{1–2}$ and $Or_{61–82}$).

Amphibole and biotite

Euhedral and subhedral calcic amphibole phenocrysts occur in trachytes, dacites, and rhyolites (Table 5). Following the nomenclature of Leake (1978), compositions are magnesiohastingsite-edenite in trachytes, and

Table 6 Representative Fe–Ti oxide compositions

Sample	2006 99	2006 99	2006 112	2006 112	2005 68	2005 68	2006 6	2006 6	2005 10	2005 10	2005 52	2005 52
Grain	mag3T	il1	mag2	il1	mag6T	il1T	mag1	il3	mag5T	il3T	mag3	il1T
Crystal type	M	M	M	M	M	M	M	M	M	M	M	M
Position	Core	Core	Core	Core	Core	Core	Core	Core	Core	Core	Core	Core
SiO_2	0.09	0.03	0.24	0.20	0.09	0.04	0.06	0.05	0.12	0.06	0.05	0.07
TiO_2	14.15	48.60	1.87	46.28	21.79	47.36	12.77	46.13	20.68	49.98	5.11	47.14
Al_2O_3	0.88	0.07	1.46	0.29	1.94	0.18	1.27	0.05	1.32	0.10	1.45	0.08
FeO(T)	76.18	44.27	86.74	43.04	69.06	46.39	78.55	47.85	74.07	47.61	84.92	49.11
MnO	0.27	0.58	0.18	0.19	0.63	0.59	0.18	0.69	0.66	0.80	1.13	2.21
MgO	0.87	3.10	0.72	0.33	1.76	2.39	0.39	0.95	1.32	2.06	0.20	0.59
Cr_2O_3	0.37	0.04	0.23	0.26	0.15	0.03	0.06	0.01	0.05	0.00	0.03	0.01
Total	92.80	96.70	91.44	90.59	95.43	96.98	93.28	95.73	98.22	100.62	92.90	99.21
X Usp	0.426		0.568		0.659		0.389		0.592		0.140	
X Ilm		0.924		0.977		0.903		0.903		0.923		0.889

M microlite

magnesiohornblende, tschermakite, edenite, and ferrohornblende in dacites and rhyolites. Some amphibole phenocrysts show normal and reverse zoning with decreasing or increasing mg# from core to rim. Most amphiboles have opaque rims due to partial reaction and breakdown.

Biotite is the most abundant ferromagnesian mineral in rhyolites and it also occurs occasionally in dacites (Table 5). Both normally and reverse-zoned crystals were found. Mg# of biotites range between 51 and 55 for dacites and 7 and 43 for rhyolites.

Fe–Ti oxides

Fe–Ti oxides are titanomagnetite and ilmenite, typically occurring as coexisting groundmass crystals and as inclusions in the other phenocrysts. Rarely, they occur as phenocrysts. Ülvospinel contents decrease from ≤83 mol % in basalt to 14–15 mol% in rhyolites; there is a correspondingly lesser change in the ilmenite content from 97 mol% to 85 mol% (Table 6).

Intensive parameters

Temperature

Magma temperatures for Süphan volcanics were estimated by using coexisting Fe–Ti oxides and two pyroxenes, plagioclase-hornblende thermometry, and plagioclase-liquid, olivine-liquid, and clinopyroxene-liquid equilibria. We have only used rim compositions of touching grains, in order to eliminate mineral pairs that were not in equilibrium with each other at the time of eruption. Fe–Ti oxide temperatures are exclusively from groundmass microlite pairs rather than phenocrysts and therefore represent most closely the temperature shortly prior to eruption, given the relatively rapid re-equilibration of this mineral pair (Venezky and Rutherford 1989). The Mg/Mn partitioning test for equilibrium (Bacon and Hirschmann 1988) applied to the coexisting oxide pairs revealed that all of those used for temperature calculations plot between error limits of Bacon and Hirschmann (1988). In mineral-liquid temperature estimations, several measurements on groundmass glasses were performed for each rock sample (Supplementary Table 2), and the averages of these measurements were used for liquid composition.

The results from these diverse methods are given in Table 7 and Fig. 6, where temperatures are plotted against the SiO_2 content of the host rock. Generally, temperatures decrease progressively from ~1,100°C in basalt to ~750°C in rhyolites, but there is significant scatter in intermediate rocks, which in some cases covers a range of almost 200°C.

In basalt sample 2006-99, a temperature estimate of 788°C derives from a single touching magnetite-ilmenite pair. As this is well below the liquidus of any basalt, regardless of H_2O content, and given that coexisting ilmenite and magnetite are rare in basalts, we suggest that this temperature comes either from a xenocrystic pair of probable rhyolitic paragenesis or underwent re-equilibration upon slow cooling of the lava flow.

Temperatures of basaltic trachyandesites are obtained from touching magnetite-ilmenite and clinopyroxene-orthopyroxene pairs, and plagioclase-liquid and clinopyroxene-liquid equilibria. Fe–Ti oxide temperatures range between 1,057 and 1,122°C. Similar temperatures are

Table 7 Temperatures estimated for Süphan magma using different methods

Method Sample	Andersen and Lindsley (1985), Stormer (1983) ilm-mag Temperature (°C)	Putirka (2008) Eq. 23 plag-liq	Putirka (2008) Eq. 33 cpx-liq	Lindsley and Frost (1992) two px	Putirka (2008) Eq. 22 ol-liq	Holland and Blundy (1994) hbl-plag	Putirka (2008) Eq. 27a kfel-plag
2006-99	788	–	–	–	–	–	–
2006-112	–	–	–	1,085	–	–	–
2005-68	1,112–1,057	950–963	971	–	–	–	–
2006-86	954–966	934–936	–	994–1,071	–	–	–
2006-6	–	–	–	919–972	–	–	–
2006-77	–	933	936	–	942	–	–
2006-8	792	–	–	912–935	–	–	–
2005-10	914–958	–	–	946–989	–	–	–
2008-4	827–894	–	–	860–891	–	829	–
2006-110	836–853	–	–	829–843	–	898	–
2005-28	802	–	–	930	–	791	–
2007-4	819 –841	882	–	–	–	–	–
2005-52	747–774	806–809	–	–	–	–	764–819
2005-69	–	895	–	–	–	–	–
2005-75	–	–	–	–	–	–	781

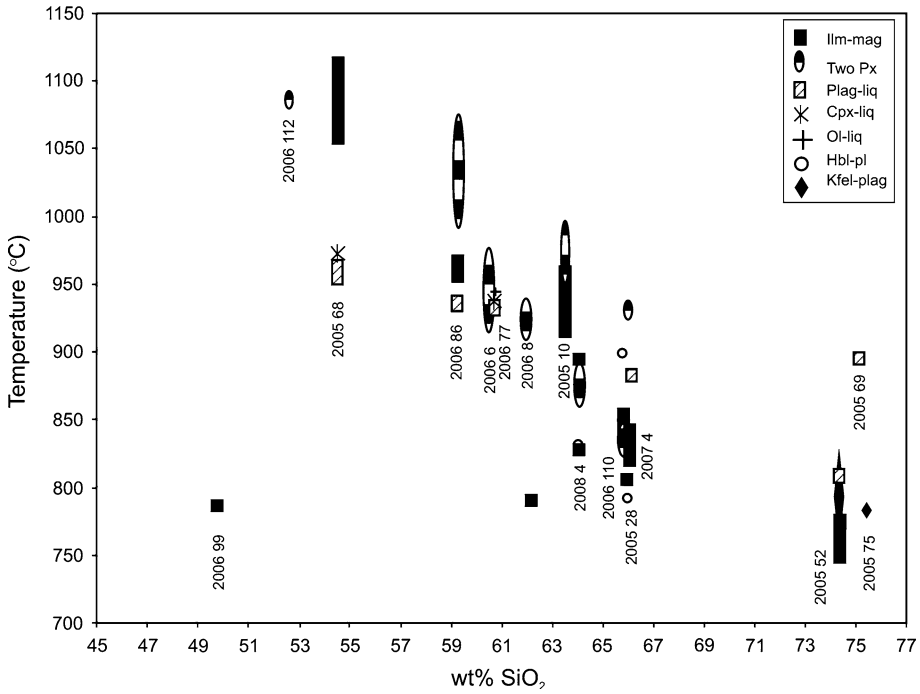

Fig. 6 Calculated temperature versus SiO_2 plot for selected Süphan volcanics. Key to abbreviations: *hbl* hornblende, *ilm* ilmenite, *kfel*: K-feldspar, *liq* liquid, *mag* magnetite, *plag* plagioclase, *px* pyroxene

obtained from touching pyroxene pairs, 1,085°C. Plagioclase-liquid and clinopyroxene-liquid thermometers overlap each other (950-962 and 971°C, respectively), but are lower than those of the mineral–mineral pairs.

In trachyandesites, temperatures were obtained from four different lavas (samples 2006-6, -8, -77, -86). Fe–Ti oxide temperatures from 2006-8 and 2006-86 and range from 792 to 966°C, with the lower temperatures from 2006-8. Temperatures decrease from sample 2006-86 to sample 2006-8 with increasing host rock SiO_2 (Fig. 6). Two-pyroxene temperatures range between 912 and 1,071°C (samples 2006-86, 2006-6, 2006-8). Plagioclase-liquid, olivine-liquid, and clinopyroxene-liquid temperatures from 2007-77 are 933, 942, and 936°C, respectively.

Generally, two-pyroxene temperatures are slightly higher than the Fe–Ti oxide temperatures.

In trachytes, temperatures are obtained from samples 2005-10 and 2008-4, with the latter generally showing lower values. Fe–Ti oxide temperatures range between 827 and 958°C; two-pyroxene temperatures 860 and 989°C. A single plagioclase-hornblende temperature from sample 2008-4 gives 829°C.

In dacites, temperatures are obtained from three different domes (2005-28, 2006-110, 2007-4). Fe–Ti oxide temperatures lie between 802 and 841°C; two-pyroxene temperatures range between 829 and 930°C; and hornblende-plagioclase temperatures are 791 and 898°C. Hornblende-plagioclase temperature of sample 2005-28 is lower than the other temperatures of the same sample, whereas hornblende-plagioclase temperature of 2006-110 is higher. Three plagioclase-liquid temperatures obtained from sample 2007-4 display an average of 882°C.

In rhyolites, Fe–Ti oxide temperatures are obtained only from sample 2005-52 and range between 747 and 774°C. These values match those of the oxide pair in the basalt sample, suggesting a possible common origin. K-feldspar plagioclase temperatures (samples 2005-52, 200-75) range from 765 to 819°C, in good agreement with oxides. Plagioclase-liquid temperatures are in the range from 806–895°C; higher temperatures belong to the older rhyolitic lava flow (2005-69).

Oxygen fugacity

Oxygen fugacity is estimated from Fe–Ti oxide equilibria using the method of Andersen and Lindsley (1985); with the recalculation scheme of Stormer (1983) (Fig. 7). Values obtained for basalt, basaltic trachyandesites, trachyandesites, and trachytes correspond to the FMQ (fayalite-magnetite-quartz) buffer. There is an apparent increase in fO_2, relative to FMQ, in the more evolved rocks. Dacites correspond to NNO ± 0.3 (nickel–nickel oxide); rhyolites to NNO+1-1.4.

Chemistry of melt inclusions and glasses

Melt inclusions and groundmass glasses offer the advantage over whole rocks of more closely approximating true liquid compositions, which may be obscured by liquid–crystal mixing processes in whole rocks, especially when they are porphyritic. Glassy melt inclusions were identified in plagioclase and olivine from basaltic trachyandesites, in orthopyroxene, plagioclase, and olivine from trachyandesites, in orthopyroxene and plagioclase from trachytes, in amphibole, orthopyroxene, and clinopyroxene from dacites, and in biotites from rhyolites. Melt inclusions in olivine, plagioclase, pyroxene, amphibole, and biotite are randomly distributed from core to rim (Fig. 8a). Some of them contain daughter crystals including Fe–Ti oxides, indicative of post-entrapment modification (Fig. 8b); such inclusions were not analyzed. We emphasize that only glassy melt inclusions without daughter crystals or demonstrable signs of post-entrapment modification were used in this study. The size of the melt inclusions is ≤150 μm. In total, 171 inclusions were analyzed (66 in olivine, 39 in plagioclase, 30 in orthopyroxene, 3 in clinopyroxene, 9 in amphibole, and 24 in biotite) together with 183 matrix glasses (Table 8 and Supplementary Table 3.) By selecting melt inclusions from a wide variety of host phenocrysts, we are able to assess any effects of post-entrapment modification, which should have a

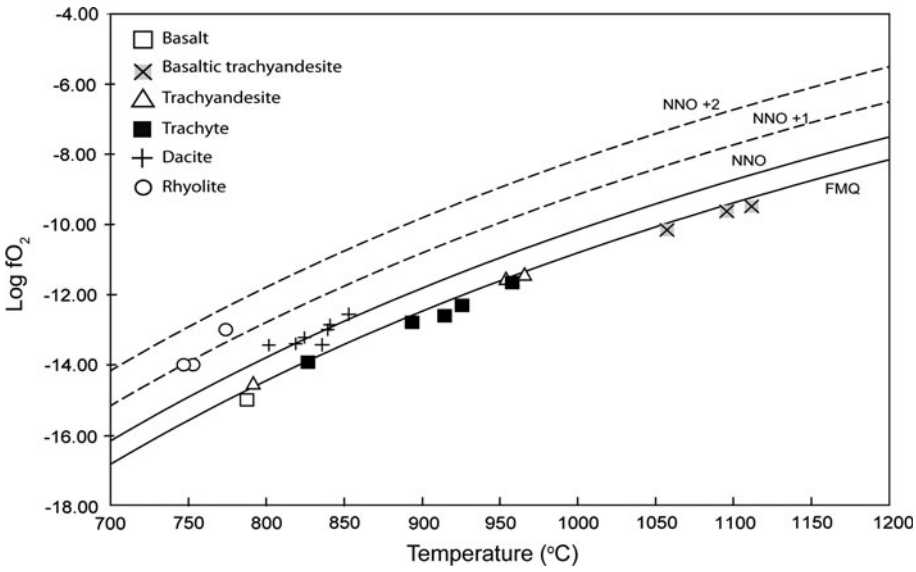

Fig. 7 Temperature versus oxygen fugacity, estimated from Fe–Ti equilibria in Süphan volcanics using the ILMAT program (Lepage 2003). Oxides were recalculated using Stormer (1983)

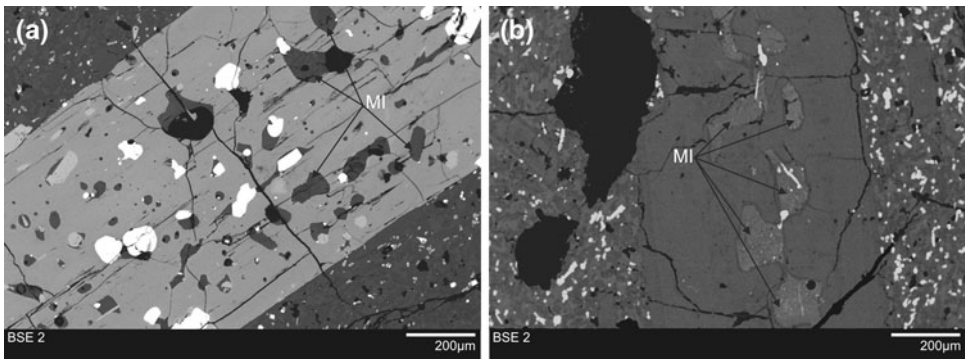

Fig. 8 Back-scatterred electron images of melt inclusions (*MIs*) in Süphan volcanics **a** MIs in orthopyroxene, randomly distributed from core to rim. **b** MIs in plagioclase, some containing daughter crystals including Fe–Ti oxides. MI with daughter crystals were not analyzed in this study

Table 8 Representative compositions of melt inclusions and matrix glasses

Melt inclusions									Matrix glasses				
Sample	2005 68 pl3	2005 68 ol1	2006 76 76_5	2006 1 6_11	2006 1 6_12	2005 10 op1	2005 28 a1	2005 28 cp1	2005 68 68G37	2006 86 G3	2005 10 G64	2005 28 G28	2005 52 G18
Host	pl	ol	ol	ol	ol	opx	amp	cpx					
SiO_2	71.10	67.96	61.48	63.00	63.07	69.46	77.42	74.29	68.43	70.48	73.09	76.63	76.41
TiO_2	1.06	1.11	0.83	1.21	1.37	0.57	0.15	0.09	1.26	1.20	0.88	0.21	0.03
Al_2O_3	12.90	16.30	17.06	15.33	15.25	14.91	12.85	12.22	14.43	13.32	12.52	10.49	11.41
FeO	1.98	2.51	1.40	2.12	1.21	1.53	1.32	0.70	2.78	3.63	2.15	0.81	0.57
MnO	0.05	0.00	0.00	0.06	0.00	0.02	0.01	0.03	0.12	0.05	0.06	0.00	0.07
MgO	0.30	0.23	0.30	0.74	0.05	0.05	0.18	0.02	0.19	0.33	0.12	0.00	0.00
CaO	0.56	2.21	0.42	2.68	0.82	0.47	0.70	0.57	1.20	0.82	0.32	0.26	0.40
Na_2O	5.10	2.97	4.42	2.96	4.99	3.49	1.65	2.36	5.32	4.06	3.77	2.26	2.56
K_2O	2.75	6.68	6.12	5.36	5.98	5.41	3.93	4.10	4.25	5.06	5.31	4.92	4.84
P_2O_5	0.36	0.41	0.42	0.23	0.36	0.02	0.00	0.01	0.23	0.24	0.04	0.05	0.03
SO_2	0.12	0.00	0.00	0.02	0.05	0.02	0.02	0.00	0.05	0.00	0.02	0.00	0.01
Cl	0.05	0.07	0.06	0.04	0.06	0.05	0.06	0.04	0.04	0.05	0.03	0.02	0.04
H_2O	3.68	0.00	7.46	6.25	6.74	4.00	1.70	5.58	1.70	0.75	1.69	4.29	3.63
Total	100.00	100.46	99.98	100.00	99.93	100.00	99.99	99.99	100.00	99.99	100.00	99.93	99.99

H_2O is estimated assuming that the missing element is H. H_2O is then included in the PAP electron microprobe data correction routine

different chemical influence for different hosts. All compositions are discussed on an anhydrous basis, although the shortfall from 100% in the analytical totals suggests dissolved volatile contents of $\leq$7.7 wt%. No direct measurements of dissolved volatiles (by SIMS or FTIR) are available. Glass chemistry is plotted in Fig. 9, alongside whole rocks for comparison.

Melt inclusions (MI) from basaltic trachyandesites range in composition from trachyandesite to rhyolite with 61–74 wt% SiO_2. The most striking feature of melt inclusions in basaltic trachyandesites is the wide range of Al_2O_3, K_2O, and Na_2O contents in the same sample. Relative to the whole rocks from Süphan, these melt inclusions are notably higher in Al_2O_3, Na_2O, and K_2O, but lower in FeO, MgO, and CaO. Matrix glasses in these rocks are trachyte to rhyolite with 65–72 wt% SiO_2. Most of them overlap with some part of the array defined by MI. However, some of them are displaced to higher FeO and TiO_2 and lower Al_2O_3 content relative to the MIs. There is rather poor correspondence between matrix glasses and even the most evolved Süphan whole rocks.

Melt inclusions and matrix glasses from trachyandesites overlap in composition, with 65–73 and 68–73 wt% SiO_2, respectively. MIs in olivines and orthopyroxenes have higher Al_2O_3 and CaO content than those in plagioclases. There is some tendency to slightly higher Al_2O_3 and TiO_2 and lower CaO and MgO to MI in trachyandesites, but for the most part there is better correspondence between MI and the more evolved end of the whole-rock trend.

Melt inclusions and matrix glasses from trachytes are rhyolitic, with 70–75 and 73–76 wt% SiO_2, respectively. MI in orthopyroxenes in these rocks have higher Al_2O_3 and CaO and lower FeO contents than MI in plagioclases, which may in part reflect differing degrees of post-

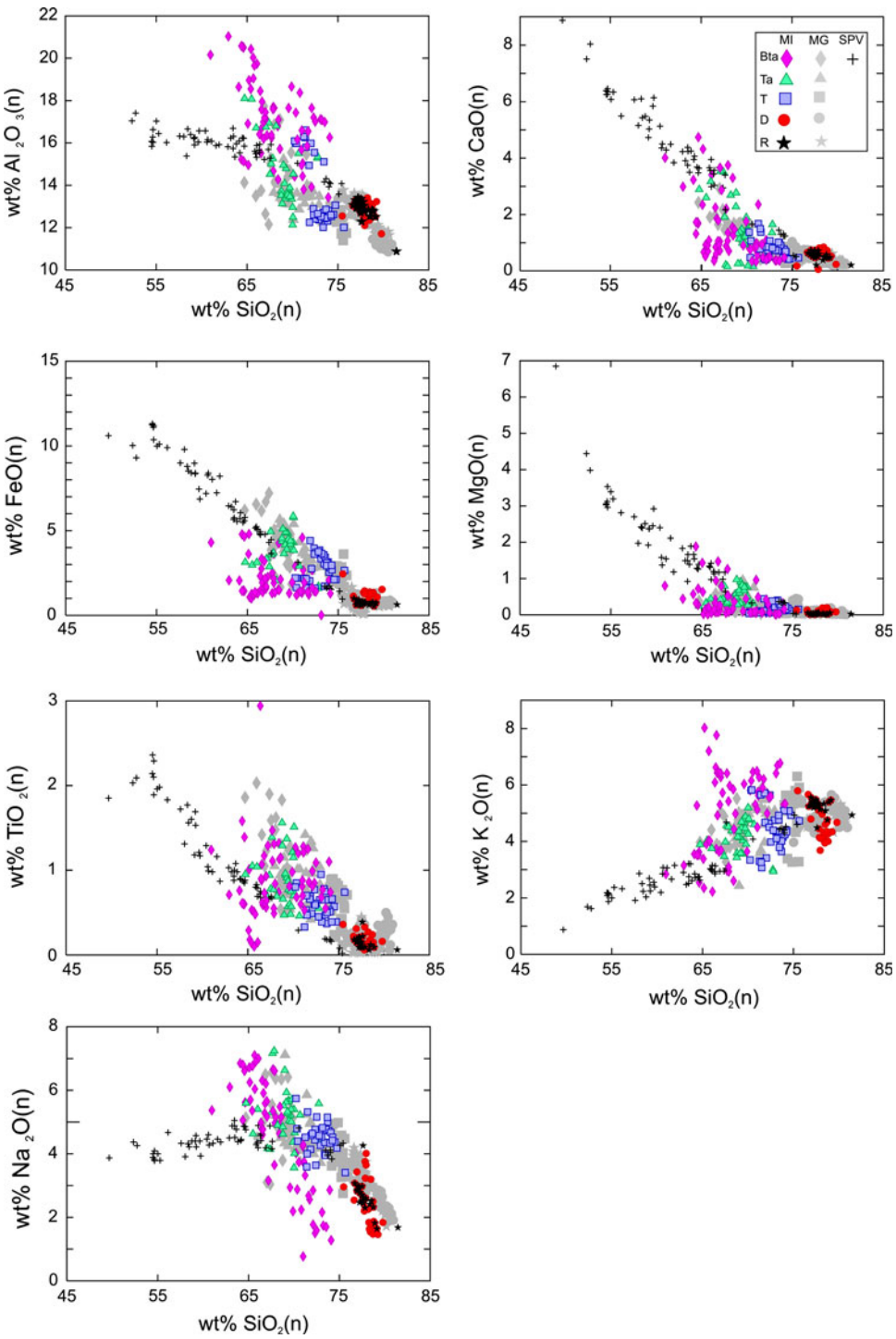

Fig. 9 Major element variation diagrams for melt inclusions, matrix glasses, and whole rocks of Süphan volcanics—(*n*) indicates anhydrous basis. *MI* melt inclusions, *MG* matrix glasses, *SPV* Süphan whole rocks, *Bta* basaltic trachyandesite host rock, *Ta* trachyandesite host rock, *T* trachyte host rock, *D* dacite host rock, *R* rhyolite host rock

entrapment crystallization of the host mineral. MI in orthopyroxenes can be grouped as low-K and high-K inclusions. There is also some bimodality in Al_2O_3, with a subordinate population of opx-hosted MI resembling those from basaltic trachyandesites with high Al_2O_3. The dominant (plagioclase-hosted) population lies close to the evolved end of the whole-rock trend, but is displaced to slightly lower Al_2O_3 and higher TiO_2.

Melt inclusions and groundmass glasses from dacites and rhyolites have very similar rhyolitic compositions with 75–81 wt% SiO_2. The lower SiO_2 end of these MI is a very good match for the most evolved whole rocks, although it is striking that the population as a whole defines a trend that is oblique to of the whole rocks, e.g., it has a flatter slope for FeO and CaO versus SiO_2, but a steeper slope for Al_2O_3.

In summary, MI and groundmass glasses, as expected, are consistently more evolved than the rocks in which they occur. However, only the least evolved MI and groundmass glasses from rhyolites and dacites consistently reproduce the composition of any Süphan whole rock. In other rocks, there are some MI that match whole rocks, but for the most part the MI compositions scatter quite widely, appearing to define trends that are quite oblique to the linear trends of the whole rocks. This is most marked in the rhyolite and dacite MI, but also apparent in trachyandesites and basaltic trachyandesites. The latter show the greatest compositional range in MI. Although some modification in chemistry due to post-entrapment crystallization around the walls of an inclusion is inevitable and likely responsible for some of the scatter, the considerable range observed in, say, Al_2O_3 or TiO_2, cannot be easily reconciled with post-entrapment crystallization of any common igneous mineral. Moreover, there is no textural evidence that the requisite amount of crystallization has occurred, either as daughter minerals or along MI walls. We suggest that variation in original melt chemistry, prior to, or during trapping, exercises the predominant control on MI composition. The important observation is that variation in composition of the MI suite taken as a whole is quite distinct from that of the whole rocks in which the inclusions are found, suggesting that MI and whole-rock chemical evolution were controlled by different processes. A final feature of the MI is the fact that compositional bimodality is observed for some host minerals in some rocks. For example, MI in trachytes show both high- and low-K_2O groups; MI in olivines from mildly alkaline basaltic trachyandesites have both high and low Na_2O and K_2O content in the same rock.

Comparison to experimental data

The mismatch between MI and whole rocks raises questions about liquid evolution at Süphan. If glasses record the composition of true (quenched) liquids, then what is the significance of the whole-rock chemical variation, notably the marked linear trends apparent in Fig. 2? We will attempt to address this question by using experimental studies to help constrain liquid lines of descent, for comparison of glass and whole-rock compositions at Süphan. A key question is the composition of the parent (basaltic) magma to chemical differentiation at Süphan. No melt inclusions were found in basaltic rocks that could lie close to original liquid compositions. As there are no experimental determinations on Süphan rocks themselves, we will use experimental studies on basalts similar in major element composition to those at Süphan. We have identified two suitable experimental studies conducted at crustal pressures, using the starting compositions shown in Fig. 2a.

In Fig. 10 Süphan data are compared to experimental melts of two volcanic rocks from the subduction-related Trans-Mexican Volcanic Belt (TMVB; Luhr 1990). Magmas from the TMVB show a number of compositional similarities to those from eastern Anatolia. One starting material is the trachyandesite erupted from El Chichón Volcano in 1982; the other is a primitive basalt erupted from Jorullo Volcano in 1759 (Fig. 2a). The 56 experiments plotted in Fig. 10 were conducted under H_2O-saturated conditions at 800–1,000°C over a range of crustal pressures (200–400 MPa). The analyzed quenched glasses reveal the possible liquid lines of descent during crustal differentiation of these starting materials (Fig. 10). They describe curved fractionation trends that culminate in liquids similar in composition to silicic magmas and melt inclusions from Süphan. These curved trends are most marked for Al_2O_3, MgO, and FeO. For Al_2O_3, there is a fractionation peak at around 63 wt% SiO_2; for MgO and FeO, there is an inflexion in the trend at $\sim$59 wt% SiO_2. The melt inclusions from Süphan basaltic trachyandesites, trachyandesites, and trachytes are well matched by the experimental glass compositions. The whole-rock compositions are not, however; they cut right across the experimental liquid lines of descent. It would appear from these experiments that differentiation from basalt to rhyolite is plausible, but not along the linear trends shown by Süphan whole rocks. Instead, the MI provide a much better match to the liquid line of descent.

The second experimental dataset is from Kerguelen large igneous province (Freise et al. 2009). Experimental melts were generated under fluid-saturated ($H_2O + CO_2$) conditions at 500 MPa, 900–1,120°C on two different basaltic compositions: tholeiitic basalt from the Northern Kerguelen Plateau and mildly alkalic basalt evolved from the Kerguelen Archipelago. In Fig. 11, we compare 74 experimental melts to whole rocks, MI, and groundmass glasses from Süphan. A very similar story emerges as for the TMVB experimental studies shown in Fig. 10. Experimental melts define curved liquid lines of descent for all oxides except CaO and K_2O, with a marked inflexion at 63 wt% SiO_2 for Al_2O_3. Although these experiments did not generate liquids with more than 66 wt% SiO_2, it is clear that the lower SiO_2 MI from Süphan provide a much better match to true liquids than do the whole rocks. This is most apparent for Al_2O_3.

In Figs. 10 and 11 show evolved magmas erupted at Süphan are consistent with generation by fractional crystallization of hydrous basalts. However, MI from Süphan provide a much better match to experimentally generated, curved liquid lines of descent than do the whole rocks with their linear chemical trends. The discrepancy between experimental liquid lines of descent and whole-rock compositions was noted previously for subduction-related magmas by Eichelberger et al. (2006) and Reubi and Blundy (2009).

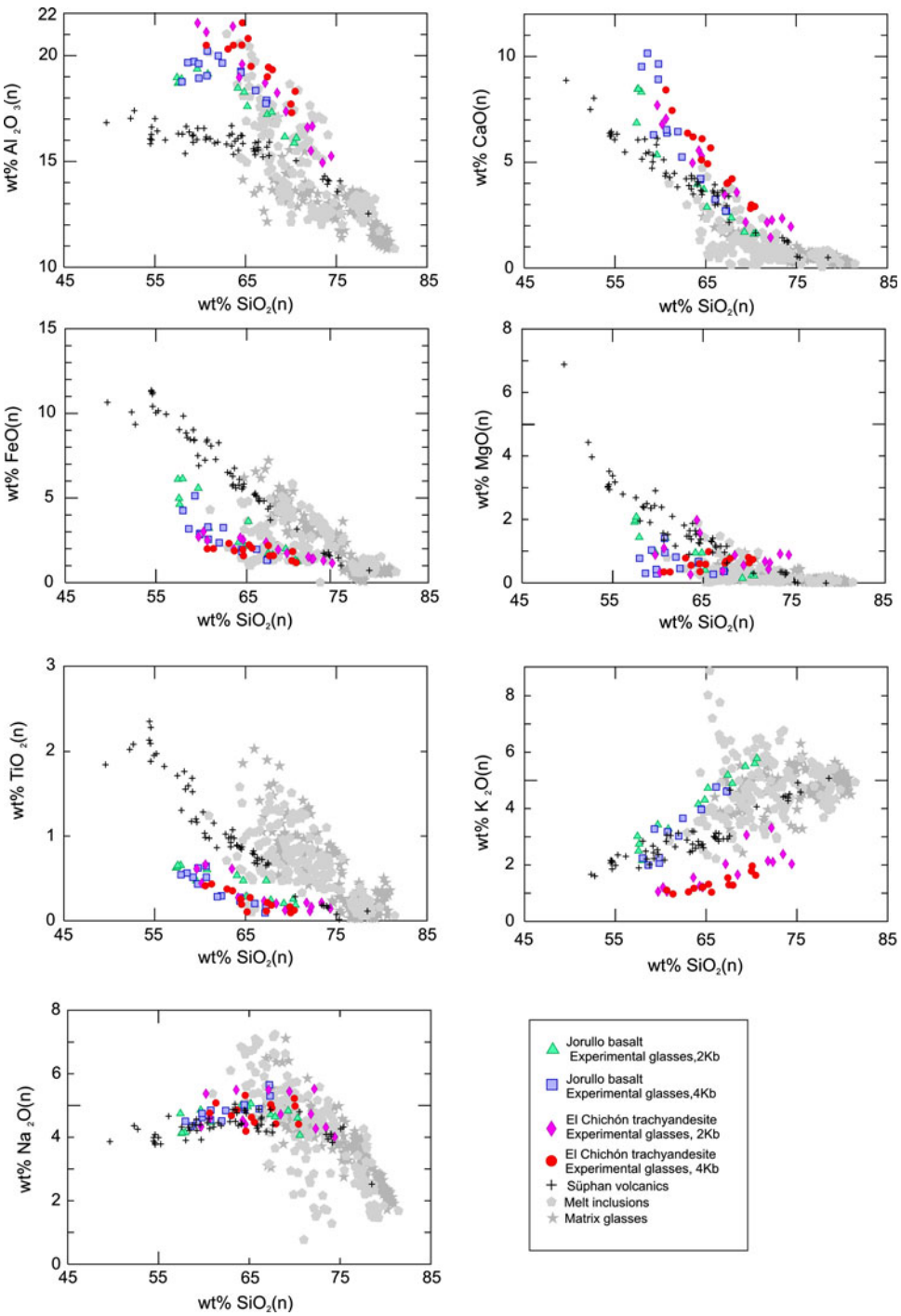

Fig. 10 Comparison of chemical variation in melt inclusions, matrix glasses, and whole rocks of Süphan volcanics (from Fig. 9) with experimentally generated melts of El Chichon tranchyandesite and Jorullo basalt from Trans-Mexican Volcanic Belt (data from Luhr 1990), whose composition are shown in Fig. 2a. (*n*) Indicates anhydrous basis

Discussion

Magma mixing

The textural complexity of the phenocrysts and the wide spread of calculated temperatures in trachytes, trachyandesites, and dacites and the linear geochemical trends are strongly suggestive of some form of mixing process in which crystals of different provenance are found in the same rock. Based on whole-rock chemistry, the two end-members involved in mixing appear to be rhyolite, with 70–75 wt% SiO_2 and at 750°C, and basaltic trachyandesite, with ~55 wt% SiO_2 and at 1,100°C. At lower SiO_2 contents, the geochemical trends are no longer linear (Fig. 2). It is therefore likely that the evolution from basalt to basaltic trachyandesite involved crystal fractionation rather than mixing. Mixing, in this context, covers a range of processes in which different melts, crystals, and magmas

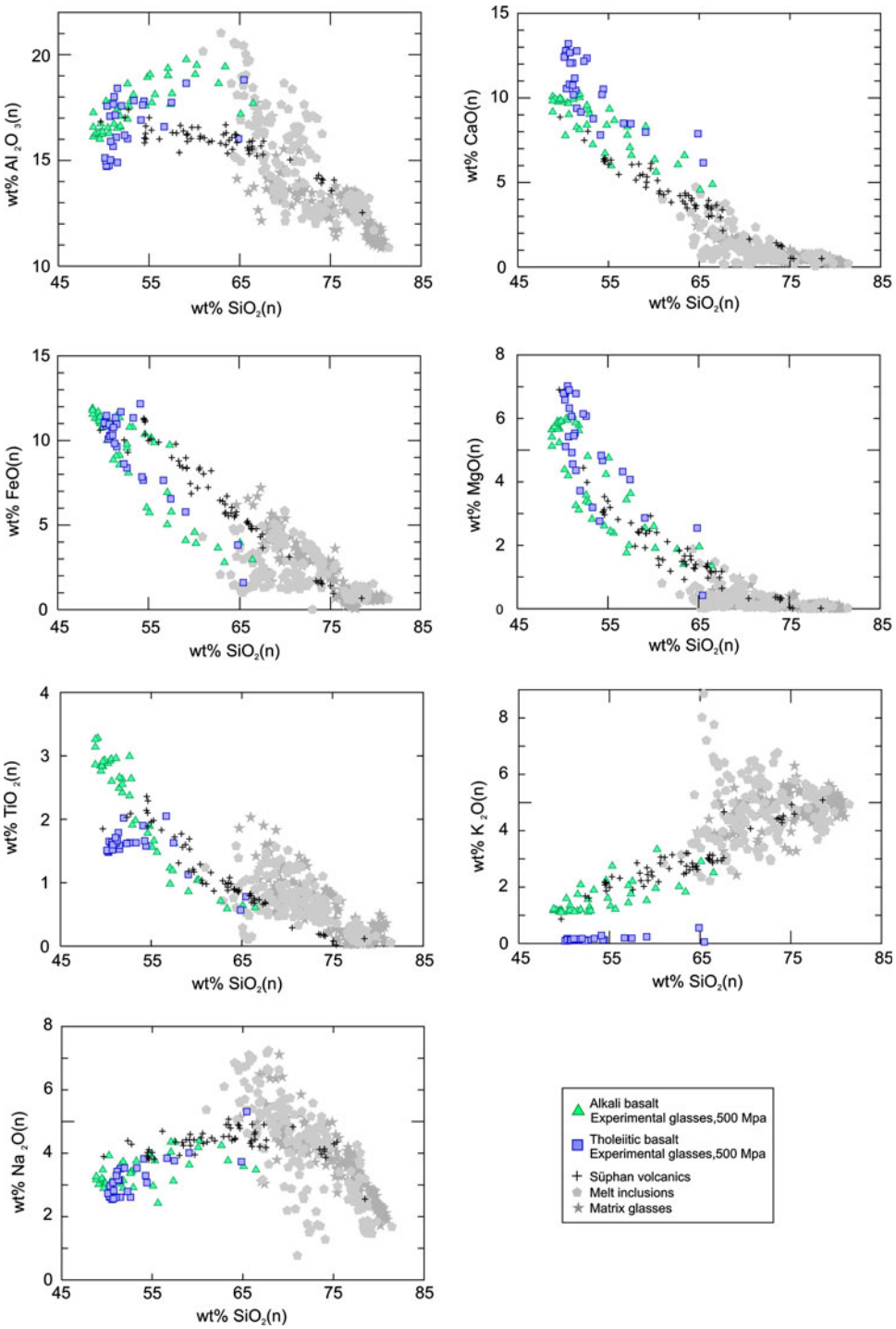

Fig. 11 Comparison of chemical variation in melt inclusions, matrix glasses, and whole rocks of Süphan volcanics (from Fig. 9) with experimentally generated melts of an alkali basalt and a tholeiite from Kerguelen Large Igneous Province (data from Freise et al. 2009), whose composition are shown in Fig. 2a. (*n*) Indicates anhydrous basis

interact. Mixing may have involved primarily the two different magma compositions given above. However, the presence of crystal clots suggests that some mixing also involved plutonic materials (i.e., solidified magmas) that became disrupted in the subvolcanic plumbing system. Crystal clots contain almost exclusively gabbroic phases such that mixing would have involved rhyolitic liquids and solidified basalts (gabbros), generating linear whole-rock trends. Disruption of the gabbros would have lead first to the formation of glomerocrysts and then to dispersed xenocrysts, with varying degrees of rim overgrowth. Such crystals are widespread in the intermediate rocks at Süphan. Interaction between newly formed magma and mafic plutonic roots has been documented recently by several authors (e.g., Dungan and Davidson 2004; Davidson et al. 2005; Bacon and Lowenstern 2005; Beard 2008;

Reubi and Blundy 2008). Reubi and Blundy (2008) describe a very similar mixing process between precursor plutonic materials and rhyolitic melts at Volcán Colima, Mexico. Their proposal, which is equally applicable to Süphan, is that the subvolcanic region contains numerous pockets of partially and fully crystallized basalts, which are encountered and disrupted by rhyolitic melts ascending through the system. Upon mixing and re-equilibration, hybrid rocks are produced. If the mixing involved only rhyolite melt and plutonic fragments, then the melt composition in the hybrid magma will be broadly rhyolitic, notwithstanding any partial resorption of xenocrysts. If mixing involves rhyolitic and basalt liquids, then hybrid melts will be produced. As mixing is likely to have occurred at shallower levels than the original differentiation, the melt phase in the hybrid rocks will be expected to follow a low-pressure crystallization trend, likely in contrast to that involved in higher pressure differentiation. This is recorded by the groundmass glasses and explains why the trends described by these glasses differ from the melt inclusion trends. It is not apparent that any further bulk magmatic differentiation accompanied crystallization of the groundmass glasses, i.e., after mixing the magmas behaved as closed systems, simply adding mass to phenocryst rims and forming microlites.

The fact that phenocryst zoning and anomalous temperatures are preserved in intermediate rocks indicates that mixing occurred on a timescale that was too short to permit full equilibration. In the case of Fe–Ti oxides, equilibration is known to occur on a timescale of days (Venezky and Rutherford 1999), suggesting that these minerals are most likely to preserve eruption temperatures. Indeed, all of our Fe–Ti oxide temperatures come from microlites rather than phenocrysts. Mixing may have occurred shortly before eruption. However, it is not possible to say at this stage whether mixing served as a trigger for eruption, as has been proposed at many other stratovolcanoes (e.g., Pallister et al. 1992; Murphy et al. 1998; Eichelberger and Izbekov 2000; Mortazavi and Sparks 2004).

Fractional crystallization

A striking feature of the Süphan rocks is the discrepancy between melt inclusion chemical trends and those of whole rocks (Fig. 9). Melt inclusions cover a wide compositional range, but lie at the evolved end of the spectrum defined by whole rocks. There are no melt inclusions with less than 61 wt% SiO_2, with the vast majority having $\geq$65 wt%. This echoes Reubi and Blundy's (2009) study of arc volcanoes worldwide, in which they found a dearth of truly silicic andesitic-dacitic melt inclusions with 60–66 wt% SiO_2, despite a wide continuum in whole-rock chemistry. The melt inclusions at Süphan derive from a wide range of host phenocryst types, which rules out post-entrapment crystallization as the *primary* source of chemical variation, although we cannot rule out some post-entrapment processes in generating scatter.

The trends described by Süphan melt inclusions are consistent with crystallization trends obtained experimentally on hydrous magmas similar in composition to the more mafic end of the Süphan whole-rock spectrum. The evidence for high Al_2O_3 in some melt inclusions is consistent with the presence of H_2O in the parent magmas responsible for these trends, which will lead to the suppression of plagioclase crystallization. The magnitude of the Al_2O_3 peak and the SiO_2 content at which it occurs are indicative of the H_2O content of the parent magma and the pressure at which crystallization occurred. The experimental data we present in Figs. 10 and 11, albeit from slightly different bulk compositions to those at Süphan, give a good match to the melt inclusions, suggesting that H_2O pressures of 200–500 MPa prevailed during crystallization. If the magmas were H_2O saturated, this would place crystallization at depths of 6–15 km beneath the volcano; greater depths are inferred for the H_2O-undersaturated case. Analysis of H_2O and CO_2 in melt inclusions is required to better constrain these depths, as would experimental studies of the Süphan rocks themselves. The melt inclusions also show high TiO_2, which is not matched by any of the experiments. This may reflect delayed onset of ilmenite or titanomagnetite crystallization at Süphan, a consequence of the lower fO_2 compared to experiments.

The melt inclusion trends do not intersect the whole-rock trends until $\sim$70 wt% SiO_2, suggesting that these are the only whole rocks more differentiated than basaltic trachyandesite that could plausibly represent true liquids. This accords with our proposal that the mixing processes that occurred beneath Süphan involved rhyolitic melts (sensu lato) and both basaltic trachyandesite liquids and gabbroic plutonic rocks.

The simplest interpretation of the discrepant whole rock and melt inclusion trends is that the crystals containing melt inclusions grew from melts that followed true fractionation trends at depth. These crystals were entrained from the source region by ascending magmas, becoming redistributed, and rimmed at shallow level by magma mixing and mingling processes. These processes served to generate linear chemical trends that almost entirely obscure the chemical variations generated by the original fractional crystallization. Some groundmass glasses have compositions similar to melt inclusions, e.g., in terms of high Al_2O_3 and TiO_2 (Fig. 9) and these may represent aliquots of liquid added to the shallow system. Piecemeal construction of a shallow magma body by repeated incursions of magmas from a deeper storage region has been documented for several large volcanic systems (e.g., Davidson and Tepley

1997; Bacon and Lanphere 2006; Charlier et al. 2008; Smith et al. 2009) and has been modeled numerically (e.g., Jellinek and DePaolo 2003; Annen 2009; Annen et al. 2008). The majority of the groundmass glasses is displaced to higher SiO_2 and appears to reflect closed-system crystallization at shallow levels following mixing.

Magmatic plumbing beneath Süphan

Our observations allow us to place some constraints on the subvolcanic magma plumbing beneath Süphan (Fig. 12). We propose a two-stage petrogenetic model, similar to that envisaged by Annen et al. (2006). Mantle-derived hydrous basalt stalls in the lower to mid-crust, whereupon it crystallizes to produce evolved melts. The thermal structure of this deep crustal hot zone is complex and evolves with time, such that it may contain a wide variety of melts of differing SiO_2 content distributed across a wide depth range. The characteristic feature of these melts is the delayed crystallization of plagioclase due to elevated H_2O, leading to high Al_2O_3 in intermediate liquids. We do not have sufficient experimental information or data on dissolved H_2O and CO_2 in melt inclusions to constrain the exact depth range over which the hot zone is developed, although we note that the crust in this region has an average thickness of 45 km and Angus et al. (2006) describe a crustal low velocity zone at ~25 km depth below Quaternary volcanic centers (e.g., Süphan, Nemrut), which most likely represents a pocket of partial melt in the middle crust. The match between experimental melts and MI (Figs. 10, 11) suggests that pressures are at least 200–500 MPa. Assimilation of older crustal rocks may accompany differentiation in the deep crust, although we require isotopic data on Süphan magmas to better evaluate this process. We venture that assimilation has had relatively little influence on the major element chemistry, given the close correspondence to experimentally generated liquid lines of descent.

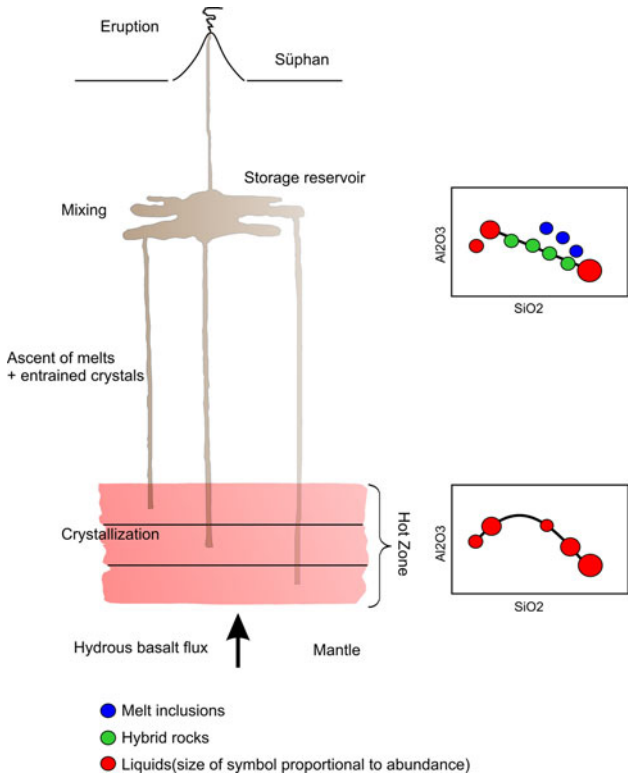

Fig. 12 Schematic representation of intracrustal magma plumbing system beneath Süphan stratovolcano (not to scale) showing that fractional crystallization predominates in the deep source region, whereas mixing processes predominate in the shallow storage region. Right hand panels show chemical variation schematically in terms of Al_2O_3 vs. SiO_2

Once generated in the deep crust, melts are buoyant due to elevated SiO_2 and H_2O and can ascend to shallower levels in the crust, plausibly entraining solid residues as they leave the hot zone. The presence of Al-rich melt inclusions of intermediate composition strongly supports crystal entrainment. These melt inclusions represent snapshots of melt evolution occurring within the hot zone. Ascending melts, with or without their cargo of entrained crystals, are arrested at shallow level where they construct a subvolcanic magma reservoir. The level of arrest may reflect the onset of H_2O saturation that leads to copious crystallization and a marked increase in viscosity (Annen et al. 2006). Without melt inclusion volatile contents, we cannot constrain the depth of the subvolcanic reservoir, although maximum volatile-by-difference estimates of melt inclusions for different rock groups range between 3.0 and 7.7 wt%, which would suggest H_2O saturation pressures of around 70–300 MPa, or 3–10 km depth. In any event, we argue that the subvolcanic reservoir is somewhat shallower than the source region.

Various melts and their entrained residues meet and interact in the shallow storage region, leading to a wide variety of mixing and mingling phenomena that define the final chemical distribution of erupted magma types. Mixing may involve contrasted magmas (e.g., rhyolite and basaltic trachyandesite) or evolved melt (rhyolite) and solidified gabbro. It is likely that both processes operated in tandem, resulting in linear whole-rock chemical trends, hybrid magmas, glomerocrysts, and dispersed, rimmed xenocrysts. It is unclear to what extent mixing and mingling served as a trigger for eruptions.

Conclusions

Mineral and whole-rock chemistry, petrography, and melt inclusion chemistry from a wide variety of rock types from Süphan stratovolcano have been used to evaluate the

relative contributions of fractional crystallization and mixing processes to compositional diversity. Although major element chemistry of Süphan volcanics shows near-continuous chemical variation from basalt to rhyolite, mineral chemistry and textures indicate that mixing processes played an important role. Intermediate magmas show a wide range of mineral compositions, for pyroxenes, olivine, and plagioclase, that are intermediate between those of basalts and rhyolites. Mineral thermometry of these rocks also yields a wide range of temperatures intermediate between rhyolite (~750°C) and basalt (~1,100°C). Consequently, the linear chemical trends shown for most major and trace elements are a product of mixing processes rather than true liquid lines of descent from a basaltic parent. In contrast, melt inclusions, hosted by a wide range of phenocryst types, display curved trends for most major elements, notably Al_2O_3, suggestive of fractional crystallization. Comparison of these trends to experimental data from basaltic and trachyandesitic magmas of similar composition to those at Süphan indicate that the melt inclusions describe true liquid lines of descent from a common hydrous parent at H_2O pressures of 200–500 MPa, although total pressure is not well constrained. Thus, the erupted magmas are cogenetic, but were generated at depths below the shallow, pre-eruptive magma storage region. We infer that chemical differentiation of a mantle-derived basalt occurred in the deep crust beneath Süphan. A variety of more and less evolved melts with ≥55 wt% SiO_2, generated in this source region, ascended to shallow level where they mixed. Mixing processes included conventional magma mixing, between contrasted melts, or mixing of crystals from ancestral, plutonic residues into evolved melts. The presence of glomerocrysts in many lavas supports the latter process. Blending of these diverse, but cogenetic minerals and melts, served to generate linear chemical trends that obscure the true liquid lines of descent in bulk rocks. The fact that chemical variation in melt inclusions reveals deeper-seated chemical differentiation indicates that inclusions were trapped in the phenocrysts prior to shallow-level blending. Groundmass glasses evolved after mixing and display trends that are distinct from those of melt inclusions. Our observations provide strong support for operation of the deep crustal hot zone hypothesis of Annen et al. (2006) in a post-collisional setting and emphasize the importance of conducting parallel petrological, geochemical, and melt inclusion studies of volcanic rocks.

Acknowledgments This work has been funded by both Middle East Technical University Scientific Research Project Foundation (ÖYP Project) and TÜBİTAK, the Scientific and Technical Research Council of Turkey (Project No. YDABAG 104Y372). YÖ also would like to thank TÜBITAK for a scholarship which allowed him to spend 10 months at Bristol in 2009. JB acknowledges European Research Council Advanced Grant 247162-CRITMAG. We are grateful to S. Kearns for his help with the electron microprobe at Bristol.

References

Andersen DJ, Lindsley DH (1985) New (and final!) models for the Ti-magnetite/ilmenite geothermometer and oxygen barometer. EOS Trans 66:416

Angus DA, Wilson DC, Sandvol E, Ni JF (2006) Lithospheric structure of the Arabian and Eurasian collision zone in Eastern Turkey from S-wave receiver functions. Geophys J Int 166(3): 1335–1346

Annen C (2009) From plutons to magma chambers: thermal constraints on the accumulation of eruptible silicic magma in the upper crust. Earth Planet Sci Lett 284:409–416

Annen C, Blundy JD, Sparks RSJ (2006) The genesis of intermediate and silicic magmas in deep crustal hot zones. J Petrol 47: 505–539

Annen C, Pichavant M, Bachmann O, Burgisser A (2008) Conditions for the growth of a long-lived shallow crustal magma chamber below Mount Pelee volcano (Martinique, Lesser Antilles Arc). J Geophys Res 113:B07209

Aydar E, Gourgaud A, Ulusoy I, Digonnet F, Labazuy P, Sen E, Bayhan H, Kurttaş T, Tolluoğlu AÜ (2003) Morphological analysis of active Mount Nemrut stratovolcano, eastern Turkey: evidences and possible impact areas of future eruption. J Volcanol Geotherm Res 123:301–312

Bacon CR, Hirschmann MM (1988) Mg/Mn partitioning as a test for equilibrium between coexisting Fe–Ti oxides. Am Mineral 73:57–61

Bacon CR, Lanphere MA (2006) Eruptive history and geochronology of Mount Mazama and the Crater Lake region, Oregon. Geol Soc Am Bull 118:1331–1359

Bacon CR, Lowenstern JB (2005) Late Pleistocene granodiorite source for recycled zircon and phenocrysts in rhyodacite lava at Crater Lake, Oregon. Earth Planet Sci Lett 233:277–293

Beard JS (2008) Crystal-melt separation and the development of isotopic heterogeneities in hybrid magmas. J Petrol 49: 1027–1041

Charlier BLA, Wilson CJN, Davidson JP (2008) Rapid open-system assembly of a large silicic magma body: time-resolved evidence from cored plagioclase crystals in the Oruanui eruption deposits, New Zealand. Contrib Mineral Petrol 156:799–813

Davidson JP, Tepley FJ III (1997) Recharge in volcanic systems: evidence from isotope profiles of phenocrysts. Science 275: 826–829

Davidson JP, Hora JM, Garrison JM, Dungan MA (2005) Crustal forensics in arc magmas. J Volcanol Geotherm Res 140:157–170

Dewey JF, Hempton MR, Kidd WSF, Şaroğlu F, Şengör AMC (1986) Shortening of continental lithosphere: the neotectonics of Eastern Anatolia—a young collision zone. In: Coward MP, Riea AC (eds) Collision tectonics. Geol Soc Lond Spec Publ, vol 19, pp 3–36

Dungan MA, Davidson J (2004) Partial assimilative recycling of the mafic plutonic roots of arc volcanoes: an example from the Chilean Andes. Geology 32:773–776

Eichelberger JC, Izbekov PE (2000) Eruption of andesite triggered by dyke injection: contrasting cases at Karymsky Volcano, Kamchatka and Mt Katmai, Alaska. Philos Trans R Soc A358: 1465–1485

Eichelberger JC, Izbekov PE, Browne PL (2006) Bulk chemical trends at arc volcanoes are not liquid lines of descent. Lithos 87:135–154

Ercan T, Fujitani T, Molsuda J, Notsu K, Tokel S, Tadahide Uİ (1990) Doğu ve Güneydoğu Anadolu Neojen-Kuvaterner volkaniklerine ilişkin yeni jeokimyasal, radyometrik ve izotopik verilerin yorumu. MTA dergisi 110:143–164

Freise M, Holtz F, Nowak M, Scoates JS, Strauss H (2009) Differentiation and crystallization conditions of basalts from the Kerguelen large igneous province: an experimental study. Contrib Mineral Petrol 158:505–527. doi:10.1007/s00410-009-0394-5

Gok R, Pasyanos ME, Zor E (2007) Lithospheric structure of the continent–continent collision zone: eastern Turkey. Geophys J Int 169:1079–1088

Grove TL, Baker MB, Price RC, Parman SW, Elkins-Tanton LT, Chatterjee N, Müntener O (2005) Magnesian andesite and dacite lavas from Mt. Shasta, northern California: products of fractional crystallization of H_2O-rich mantle melts. Contrib Mineral Petrol 148:542–565

Hildreth W, Moorbath S (1988) Crustal contributions to arc magmatism in the Andes of Central Chile. Contrib Mineral Petrol 98:455–489

Holland T, Blundy JD (1994) Non-ideal interactions in calcic amphiboles and their bearing on amphibole-plagioclase thermometry. Contrib Mineral Petrol 116:433–447

Humphreys MCS, Kearns SL, Blundy JD (2006) SIMS investigation of electron-beam damage to hydrous, rhyolitic glasses: implications for melt inclusion analysis. Am Mineral 91:667–679

Innocenti F, Mazzuoli R, Pasquare G, Redicat di Brozolo F, Villari L (1976) Evolution of the volcanism in the area of interaction between the Arabian, Anatolian and Iranian plates (Lake Van, Eastern Turkey). J Volcanol Geotherm Res 1:103–112

Innocenti F, Mazzuoli R, Pasquare G, Serri G, Villari L (1980) Geology of the volcanic area north of Lake Van (Turkey). Geol Runds 69:292–322

Irvine TN, Baragar WRA (1971) A guide to the chemical classification of the common volcanic rocks. Can J Earth Sci 8:523–548

Jellinek AM, DePaolo DJ (2003) A model for the origin of large silicic magma chambers: precursors of caldera-forming eruptions. Bull Volcanol 65:363–381

Karaoğlu Ö, Özdemir Y, Tolluoğlu AÜ, Karabıyıkoğlu M, Köse O, Froger JL (2005) Stratigraphy of the volcanic products around Nemrut Caldera: implications for reconstruction of the Caldera Formation. Turk J Earth Sci 14:123–143

Keskin M (2003) Magma generation by slab steepening and breakoff beneath a subduction-accretion complex: an alternative model for collision-related volcanism in Eastern Anatolia, Turkey. Geophys Res Lett 30(24):1–4. doi:10.1029/2003Gl018019

Keskin M (2007) Eastern Anatolia: a hot spot in a collision zone without a mantle plume. In: Foulhrt GR and Jurdy D (eds) Plates, plumes, and planetary processes. Geol Soc Am Spec Pap, vol 430, pp 693–722

Keskin M, Pearce JA, Mitchell JG (1998) Volcano-stratigraphy and geochemistry of collision-related volcanism on the Erzurum-Kars Plateau, North Eastern Turkey. J Volcanol Geotherm Res 85:355–404

Kheirkhah M, Allen MB, Emami M (2009) Quaternary syn-collision magmatism from the Iran/Turkey borderlands. J Volcanol Geotherm Res 182:1–12. doi:10.1016/j.jvolgeores.2009.01.026

Le Bas MJ, Le Maitre RW, Streckeisen A, Zannettin B (1986) A classification of volcanic rocks based on the total alkali-silica diagram. J Petrol 27:745–750

Leake BE (1978) Nomenclature of amphiboles. Am Mineral 63:1023–1052

Lepage LD (2003) ILMAT: an excel worksheet for ilmenite-magnetite geothermometry and geobarometry. Comp Geosci 29:673–678

Lindsley DH, Frost BR (1992) Equilibria among Fe–Ti oxides, pyroxenes, olivine, and quartz: part I. Theory. Am Mineral 77:987–1003

Luhr JF (1990) Experimental phase relations of water- and sulfur-saturated arc magmas and the 1982 eruptions of El Chichón Volcano. J Petrol 31:1071–1114

Miyashiro A (1978) Nature of alkalic volcanic rocks series. Contrib Mineral Petrol 66:91–104

Mortazavi M, Sparks RSJ (2004) Origin of rhyolite and rhyodacite lavas and associated mafic inclusions of Cape Akrotiri, Santorini: the role of wet basalt in generating calcalkaline silicic magmas. Contrib Mineral Petrol 146:397–413

Murphy MD, Sparks RSJ, Barclay J et al (1998) The role of magma mixing in triggering the current eruption at the Soufrière Hills volcano, Montserrat, West Indies. Geophys Res Lett 25:433–3436

Nakamura N (1974) Determination of REE, Ba, Mg, Na and K in carbonaceous and ordinary chondrites. Geochim Cosmochim Acta 38:757–775

Notsu K, Fujitoni T, Ui T, Matsuda J, Ercan T (1995) Geochemical features of collision related volcanic rocks in central and Eastern Anatolia, Turkey. J Volcanol Geotherm Res 64:171–192

Ogata A, Nakamura K, Nagao K, Akimoto S (1989) K-Ar age of young volcanic rocks of Turkey. 1989 annual meeting of the Geochemical Society of Japan ICO 3

Özacar AA, Gilbert H, Zandt G (2008) Upper mantle discontinuity structure beneath East Anatolian Plateau (Turkey) from receiver functions. Earth Planet Sci Lett 269:426–434

Özdemir Y, Karoğlu Ö, Tolluoğlu AÜ, Güleç N (2006) Volcanostratigraphy and petrogenesis of the Nemrut stratovolcano (East Anatolian High Plateau): the most recent post-collisional volcanism in Turkey. Chem Geol 226:189–211

Özdemir Y, Karoğlu Ö, Tolluoğlu AÜ, Güleç N (2007) Reply to discussion by Evren Çubukçu, Erkan Aydar and Alain Gourgaud of Volcanostratigraphy and petrogenesis of the Nemrut stratovolcano (East Anatolian High Plateau): the most recent post-collisional volcanism in Turkey. Chem Geol 245:130–134

Pallister JS, Hoblitt RP, Reyes JP (1992) A basalt trigger for the 1991 eruption of Pinatubo volcano. Nature 356:426–428

Pearce JA (1983) The role of sub-continental lithosphere in magma genesis at destructive plate margins. In: Hawkesworth CJ, Norry MJ (eds) Continental basalt and mantle xenolits. Shiva Publishing Limited, Cheshire, pp 230–249

Pearce JA, Bender JF, De Long SE, Kidd WSF, Low PJ, Güner Y, Şaroğlu F, Yılmaz Y, Moorbath S, Mitchell JG (1990) Genesis of collision volcanism in Eastern Anatolia, Turkey. J Volcanol Geotherm Res 44:189–229

Putirka KD (2008) Thermometers and barometers for volcanic systems. In: Putirka KD and Tepley F (eds) Rev Mineral Geochem, vol 69, pp 61–120

Reubi O, Blundy JD (2008) Assimilation of plutonic roots, formation of high-K "exotic" melt inclusions and genesis of andesitic magmas at Volcán de Colima, Mexico. J Petrol 49:2221–2243

Reubi O, Blundy JD (2009) A dearth of intermediate melts at subduction zone volcanoes and the petrogenesis of arc andesites. Nature 461:1269–1273

Sandvol E, Türkelli N, Barazangi M (2003a) The eastern Turkey seismic experiment: the study of a young continent-continent collision. Geophys Res Lett 30. doi:10.1029/2003GL018912

Sandvol E, Türkelli N, Zor, E, Gök R et al (2003b) Shear wave splitting in a young continent–continent collision: an example from Eastern Turkey. Geophys Res Lett 30. doi:10.1029/2003GL017390

Şen PA, Temel A, Gourgaud A (2004) Petrogenetic modeling of quaternary post-collisional volcanism: a case study of central and eastern Anatolia. Geol Mag 141:81–98

Şengör AMC, Kidd WSF (1979) Post-collisional tectonics of the Turkish-Iranian plateau and a comparison with Tibet. Tectonophysics 55:361–376

Şengör AMC, Özeren S, Genç T, Zor E (2003) East Anatolian high plateau as a mantle supported, north-south shortened domal structure. Geophys Res Lett 30. doi:10.1029/2003GL017858

Şengör AMC, Özeren S, Keskin M, Sakınç M, Özbakir AD, Kayan I (2008) Eastern Turkish high plateau as a small Turkic-type orogen: Implications for post-collisional crust-forming processes in Turkic-type orogens. Earth Sci Rev 90:1–48

Smith VC, Blundy JD, Arce JL (2009) A temporal record of magma accumulation and evolution beneath Nevado de Toluca, Mexico, preserved in plagioclase phenocrysts. J Petrol 50:405–426. doi:10.1093/petrology/egp005

Stormer JC Jr (1983) The effects of recalculation on estimates of temperature and oxygen fugacity from analyses of multicomponent iron-titanium oxides. Am Mineral 68(5–6):586–594

Tchalenko JS (1977) Reconnaissance of seismicity and tectonics at northern border of Arabian plate (Lake Van region). Rev Geogr Phys Geol Dyn 19:89–207

Venezky DY, Rutherford MJ (1999) Petrology and Fe–Ti oxide reequilibration of the 1991 Mount Unzen mixed magma. J Volcanol Geotherm Res 89:213–230

Yılmaz Y, Şaroğlu F, Güner Y (1987) Initiation of the neomagmatism in East Anatolia. Tectonophysics 137:177–199

Yılmaz Y, Güner Y, Şaroğlu F (1998) Geology of the quaternary volcanic centres of the East Anatolia. J Volcanol Geotherm 85:173–210